OPTICAL PROPERTIES OF $RbMnF_3:Er^{3+}$

By

MARK VERNON IVERSON

Bachelor of Arts

Luther College

Decorah, Iowa

1975

Submitted to the Faculty of the Graduate College
of the Oklahoma State University
in partial fulfillment of the requirements
for the Degree of
DOCTOR OF PHILOSOPHY
July, 1979

OPTICAL PROPERTIES OF $RbMnF_3:Er^{3+}$

Thesis Approved:

W. A. Sibley
Thesis Adviser

Lin G Rockley

Larry E. Hallibuton

Richard C. Powell

Norman N. Durham
Dean of the Graduate College

ACKNOWLEDGMENTS

The author wishes to express his appreciation to his major adviser, Dr. William A. Sibley, for his professional guidance, assistance, and time for discussion throughout the course of this study. A great deal of credit must also be given to Dr. J. J. Martin for growing the crystals used in this study. In addition to the above two individuals thanks are extended to Drs. R. C. Powell, L. E. Halliburton, N. Koumvakalis, L. Merkle, M. Rockley, A. Podinsh, and P. Westhaus for their helpful ideas. Thanks are also extended to Mr. Heinz Hall and the members of the Physics-Chemistry Machine Shop staff for their excellent work. Mrs. Dolores Behrens is appreciated for her excellent typing of the final draft. Financial support provided by the 3M Company and the National Science Foundation for various portions of this work is gratefully acknowledged.

Special gratitude is expressed to my parents for their support and guidance through the years. Finally but most importantly, the author wishes to express his love and gratitude to his wife, Rachel, and to dedicate this thesis to his infant son Nathaniel.

TABLE OF CONTENTS

LIST OF TABLES

LIST OF FIGURES

CHAPTER I

INTRODUCTION

The optical properties of a crystalline solid may be modified by the introduction of defects. This process makes possible the development of technologically important devices such as lasers or upconverting phosphors. Impurity defects such as rare earth or transition metal ions can be introduced into the lattice during the crystal growth. External methods such as additive coloration (1,2), electrolytic coloration (1,3), or exposure to ionizing or particle radiation (4) may introduce additional defects or change existing impurity defects. Becquerel (5) was the first to spectroscopically examine the multitude of sharp rare earth impurity lines at low temperatures. In the 1930's theoretical work by Bethe (6), Kramers (7), and Van Vleck (8) provided an interpretation and explanation of the origin for rare earth spectra. The next major thrust came in the early 1960's when Dieke (9,10) generated a complete set of energy level assignments for all the trivalent rare earths in the anhydrous triclorides. Excellent reviews are available describing 4f wavefunctions and their interaction with the lattice (11-13).

The marked color differences of the same crystal with different divalent transition metal impurities gave early investigators strong evidence that the local symmetry around the 3d ion was important.

Bethe (14) was the first to use group theoretical arguments to show that the degeneracies of a free ion were removed in fields of cubic or lower symmetry. Van Vleck (15) and Finkelstein and Van Vleck (16) were the first to apply crystal field theory to optical spectra of d electrons in paramagnetic crystals. Hartman, Schlaefer, and Ilse (17-19) used crystal field theory to calculate the energy levels of 3d transition metals which contain no more than five d electrons. Further work by Orgel (20-22), Tanabe, Surgano and Kamimura (23-24), Ballhausen (25), Owen (26), and Griffith (27) has built an excellent theoretical base for 3d transition metal ions.

The optical properties due to transition metal ions such as Ni^{2+}, Mn^{2+}, or Co^{2+} in a simple cubic perovskite structure have been experimentally studied by numerous researchers (28-31). An example of the perovskite structure for $RbMnF_3$ is shown in Figure 1. Early experimental studies (32-34) used low temperature optical absorption spectra to find the crystal field strength and to assign the various absorption bands. Emission studies (35-38) followed with the observation of a strong temperature dependence to the integrated fluorescent intensity and lifetime. Since $RbMnF_3$ is antiferromagnetic below the Néel temperature, this strong temperature dependence in the emission was originally interpreted as being due to a local lattice distortion coupled with the magnetic interaction of excited Mn^{2+} ions. Later Green et al. (39) and Gooen et al. (40) found that energy transfer was the active process with emission originating from Mn^{2+} sites perturbed by nearby impurities. Further evidence for energy transfer has been found in the system $RbMn_xMg_{1-x}F_3$ where it was demonstrated

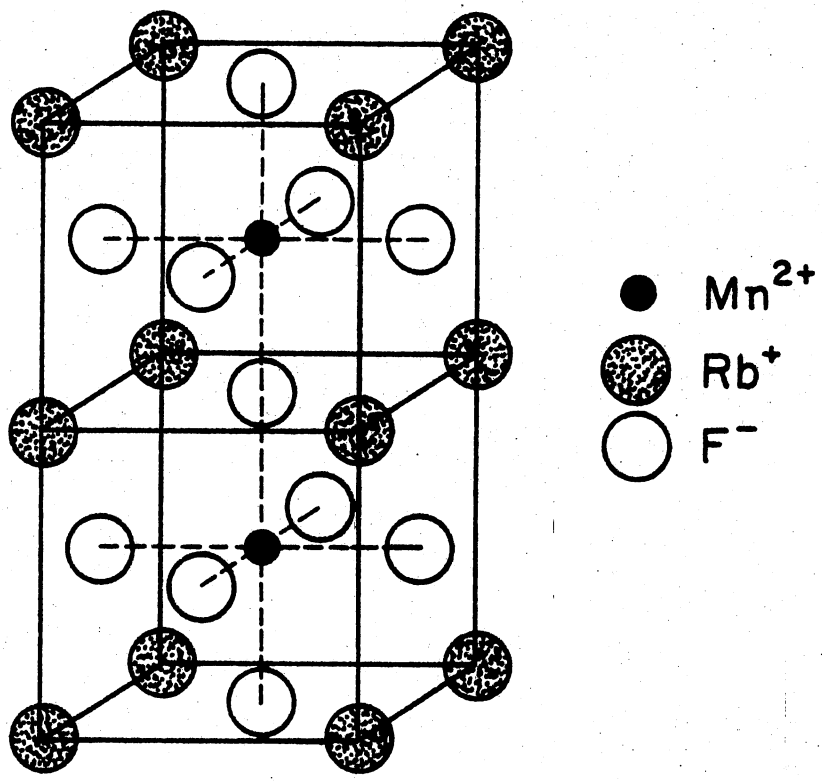

Figure 1. Perovskite Structure of $RbMnF_3$

that the energy transfer process could be stopped for crystals containing less than 20% Mn^{2+} (41). In additional experimentation, defects were photochemically introduced by irradiation with 1.5 M.e.V. electrons. These defects acted as perturbed manganese traps (42). An excellent review of the unirradiated perturbed manganese emission has been given by Imbusch (43).

Sensitized emission from isolated rare earth impurity defects can be obtained by energy transfer from a transition metal ion. Emissions of this type from Nd^{3+} in $RbMnF_3$ (40,44), Er^{3+} in MnF_2 (45-48), Eu^{3+} in MnF_2 (48-50), and from Eu^{3+} in $KMnF_3$ (51-52) have been observed and analyzed. Flaherty and Di Bartolo (45-46) found for $MnF_2:Er^{3+}$ that delocalized energy was transferred nonradiatively to the Er^{3+}. Emission has not been observed from the $^4S_{3/2}$ level of Er^{3+} even though its position may be determined under laser excitation (48).

Thus the purpose of this study is to investigate the radiative, radiationless, and energy transfer properties of $RbMnF_3:Er^{3+}$. Radiationless relaxation is discussed in terms of the phenomenological model of Struck and Fonger (53-57) and compared with the values obtained from Flaherty and Di Bartolo's model (46). In addition, the properties of irradiated $RbMnF_3:Er^{3+}$ are also investigated. In both cases, comparisons are made with the undoped material when it is possible. Chapter II discusses some of the theory for ions in a solid. The third chapter is a discussion of experimental apparatus and procedure. Actual doping levels are also discussed in that section. The fourth chapter explains the experimental results in the irradiated and unirradiated cases so that they may be discussed in the fifth chapter.

Finally the last chapter considers the key results and suggests problems for future study.

CHAPTER II

THEORETICAL BACKGROUND

Energy Levels for an Ion in a Crystal

The energy levels for a localized point defect or ion in a crystal can be found theoretically by solving Schrodinger's equation with the following Hamiltonian (58):

$$H = \frac{-\hbar^2}{2m} \sum_i \nabla_i^2 - \sum_i \frac{Ze^2}{r_i} + \sum_{i>j} \frac{e^2}{r_{ij}} + \sum_i C(r_i)\bar{\ell}_i \cdot \bar{s}_i + H_c \qquad (1)$$

These terms are respectively the kinetic energy of the electrons, the electrostatic interaction of the electrons with the nucleus of charge $Z|e|$, the interelectron electrostatic repulsion, the spin-orbit interaction, and the interaction of the ion with surrounding neighbors or crystalline field (H_c). The sums are over the number of electrons bound to the ion. The r_i vector is a vector from the nucleus to the ith electron and $r_{ij} = |r_i - r_j|^{-1}$. Clearly the first two terms in the Hamiltonian are just a central field problem; while, the first four terms represent the Hamiltonian for a free ion.

For transition metal ions such as Ni^{2+} and Mn^{2+}, the crystal field interaction in Equation 1 is much stronger than the spin-orbit interaction. The relative magnitude of H_c to the interelectron

repulsion term is usually not known from first principles. Thus two cases may be considered. The first is to assume that H_c is much weaker than the interelectron coupling. The 3d electrons are then coupled together to form various ^{2S+1}L terms for which $\Sigma_i r_{ij}^{-1}$ is diagonal. The matrix elements of H_c are then found between these states. This procedure is often referred to as the weak field scheme. The various terms for Mn^{2+} have been tutorially enumerated by Yun (59). Orgel's (20) calculated ^{2S+1}L weak field term energies are shown on the left side of Figure 2. The other extreme is to assume that H_c is much bigger than the interelectron repulsion. In this case the electrons are placed in configurations which diagonalize H_c and result in terms of the form $^{2S+1}\Gamma$ where Γ is a group theoretical symbol which represents the symmetry of the level. Matrix elements are then calculated using $\Sigma_i e^2 r_{ij}^{-1}$ between these various terms. This case is usually referred to as the strong field case. Again the various calculated terms are shown on the right side of Figure 2.

The corresponding states on each side of Figure 2 are then correlated (60) and energetically fit to absorption peak energies to determine assignments and a value for the crystal field (33). These assignments and energies are plotted on the upper right hand portion of Figure 3. The letters of the alphabet are traditional and refer to earlier work by Mehra and Vehkateswarlu (32).

In rare earth ions such as Er^{3+}, the spin orbit interaction term in Equation 1 is much stronger than the crystal field interaction. The orbital radius of the 4f electrons is half of the ionic radius due to the filling of the 5s and 5p orbitals. These 5s and 5p orbitals

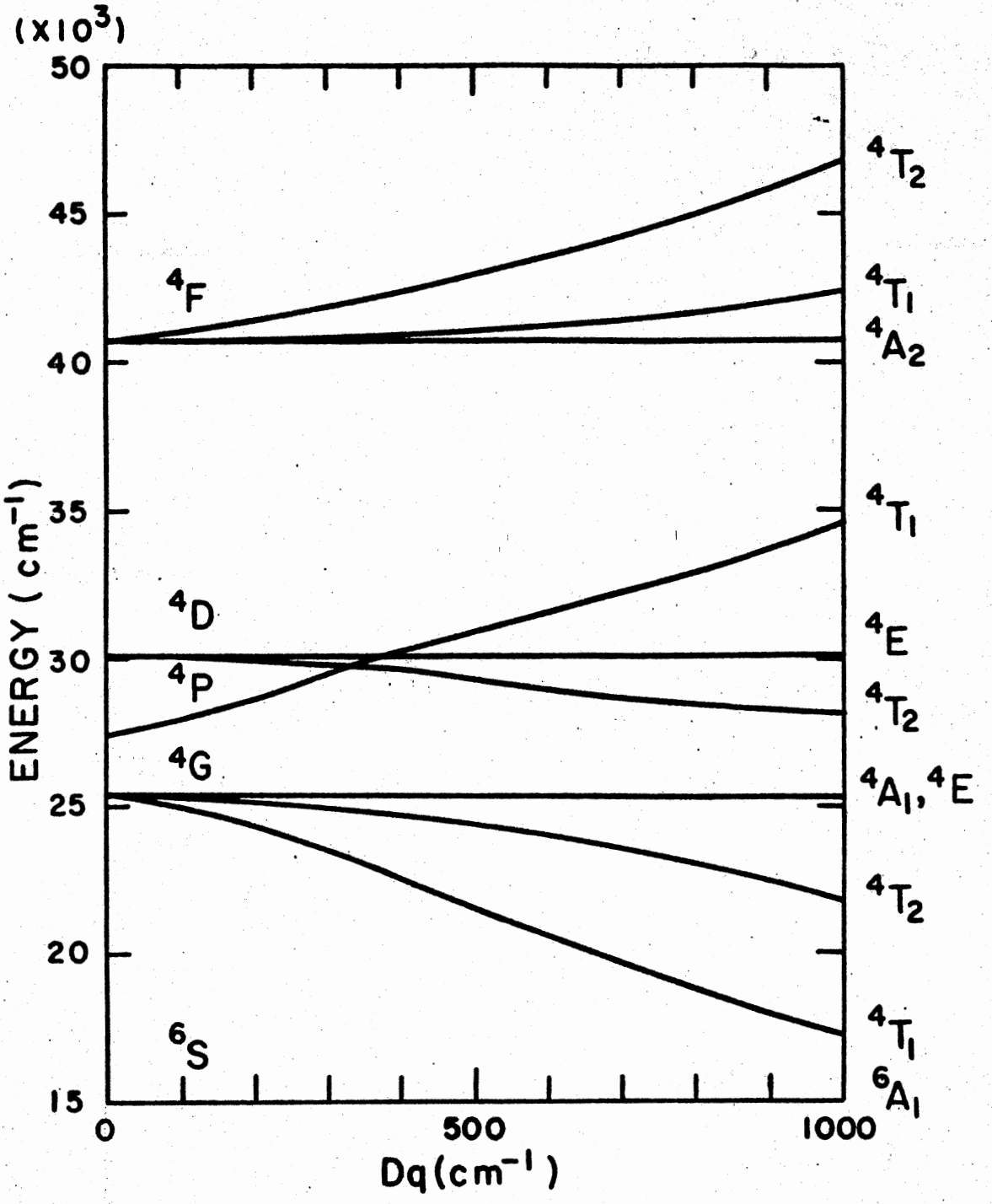

Figure 2. Energy Level Diagram for Mn^{2+}

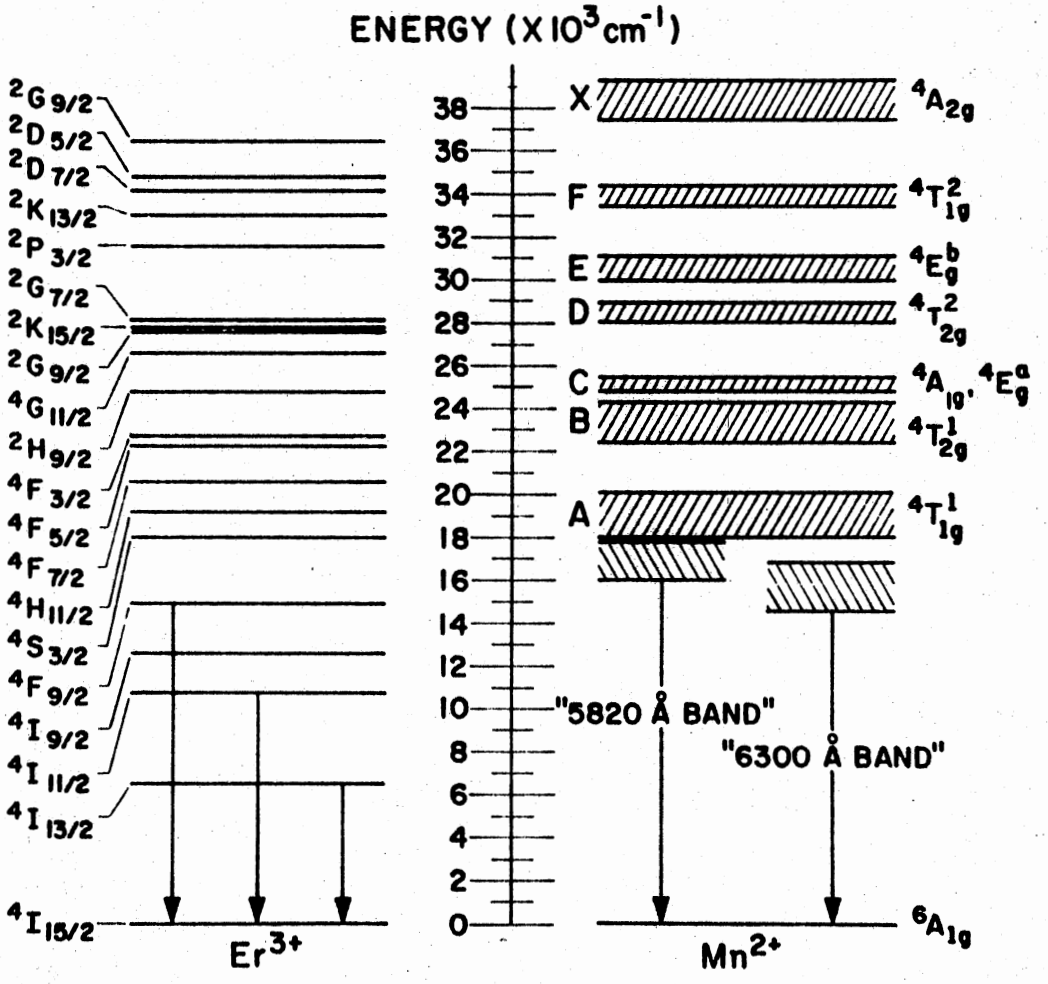

Figure 3. Partial Energy Level Diagram for Mn^{2+} and Er^{3+}

shield the 4f electrons in such a way that the gross optical properties are almost independent of the host crystal for a given ion. Clearly the energy levels for this case can be represented by free ion terms of the form $^{2S+1}L_J$. With this in mind, the energy levels for Er^{3+} in $RbMnF_3$ are shown on the left side of Figure 3.

Energy Transfer Processes

So far, the absorption and emission of light has been assumed to take place at single defect sites. Experimental evidence shows, however, that there are a number of cases where two or more defects contribute to the absorption or emission process. The term energy transfer process usually refers to an excited sensitizer defect or ion transferring its excitation energy to another defect called the activator. A second class of less frequent processes is also possible where two or more ions cooperate to absorb or emit one photon. Detailed treatments of the work presented in this section are found in the following excellent reviews (61-64,11).

On the left side of Figure 4 the energy levels of a sensitizer ion are shown. The sensitizer emission band overlaps with the activator absorption band. There is the possibility that the emission may be radiatively reabsorbed. This behavior is easily recognized and of less importance than the nonradiative energy transfer from S→A. Förster and Dexter (65-66) have worked out the following expression for the rate of nonradiative energy transfer for S→A:

$$P_{SA} = \frac{2\pi}{\hbar} |\langle S^* A|H_{int}|S A^*\rangle|^2 \int g_s(w)\, g_A(w)dw \qquad (2)$$

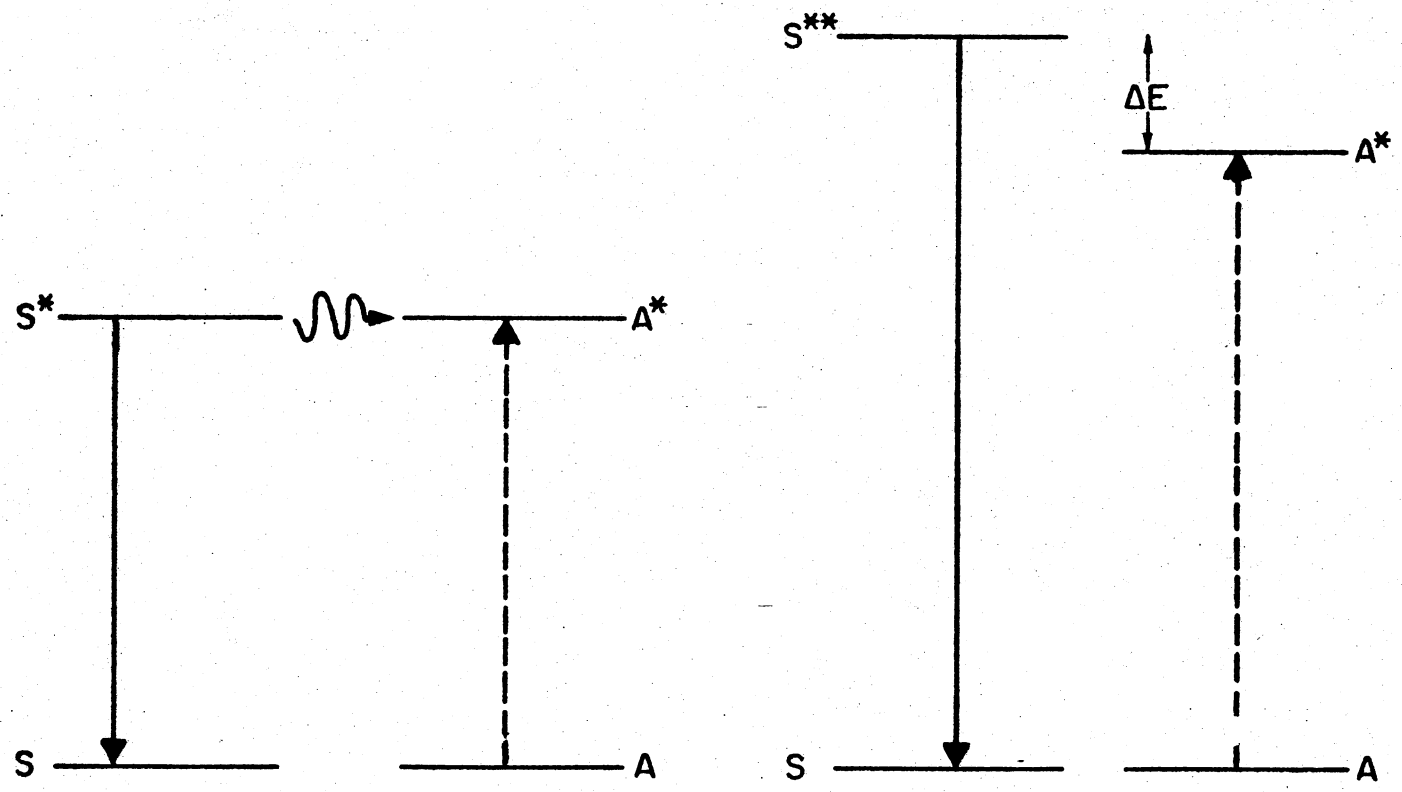

Figure 4. Resonant and Phonon Assisted Energy Transfer

where the quantum numbers for the states are S and A. $g_S(w)$ and $g_A(w)$ are the two spectral line shape functions of the transition $S^* \rightarrow S$ and $A \rightarrow A^*$. This formula is only valid for resonant energy transfer because the integral containing the overlap of the sensitizer and activator emission bands goes to zero when they are far apart. The interaction Hamiltonian is usually written in terms of an electric multipole or exchange interaction. The resultant range dependence of the energy transfer probability P_{SA} is

$$P_{SA} = \frac{1}{\tau_S^o}\left(\frac{R_o}{R}\right)^n \qquad (3)$$

where n=6 for dipole-dipole interaction, n=8 for dipole quadrapole interactions and n=10 for quadrapole-quadrapole interactions. τ_S^o is the lifetime of the sensitizer without the activator while R_o is the critical transfer distance which is proportional to the overlap integral in Equation 2 to the one over n power. For an exchange interaction the energy transfer rate is proportional to $e^{-2z(\ell nS)}$ where z is the number of ligands and S corresponds to the wave function overlap integral.

When there is an energy difference (ΔE) between S^{**} and A^* as shown on the right side of Figure 4, phonon assisted energy transfer may occur. The theory for this case was first developed by Orbach (67) and worked out in detail later by Miyakawa and Dexter (68) and Orbach (69). The following formula is given by Orbach:

$$P_{SA} = \frac{2\pi}{h}|< S^*A|H_{int}|SA^*>|^2 K\left\{\begin{matrix} n \\ n+1 \end{matrix}\right\}\int g_S(w)\ g_A(w \pm \hbar\omega)dw \qquad (4)$$

where K is a combination of electron-phonon matrix elements, n is the phonon occupation number and the plus and minus signs respectively refer to phonon absorption or emission in the energy transfer process. There is still some disagreement about the exact evaluation of K(11). Experimental studies in the past have tended to concentrate on phonon assisted energy transfer between ions with similar electron phonon coupling. Clearly phonon assisted energy transfer studies between isolated transition metal and rare earth ions might clarify this discrepancy.

As the concentration of sensitizer ions is increased, the possibility of S→ S transfer increases. In this case the quantum efficiency is changed due to the fact that the excitation of a S ion far away from an A ion can be reached via the intervening S ions. The A ions are said to act as traps which draw the excitation energy away from the S ions. The S→S transfer rate is also dependent on the type of ion present. Rare earth ions couple very weakly even at high concentrations while 3d ions such as Cr^{3+} or Mn^{2+} can couple quite strongly which results in a noticeable concentration effect.

$RbMnF_3$ obviously has a high concentration of Mn^{2+}. In this case the excitation of the manganese is a property of the crystal rather than a single ion. Imbusch (43) has mathematically described this rapid traveling between Mn^{2+} as an "exciton" theory. For our purposes it suffices to note that this energy may be transferred through the exciton band to impurity perturbed Mn^{2+} traps, other ions such as Er^{3+} or radiation induced traps as portrayed on Figure 5. The possibility also exists for these traps to thermally repopulate the exciton band. Finally it should be noted that the two emission bands shown in Figure 3 are impurity perturbed emission bands.

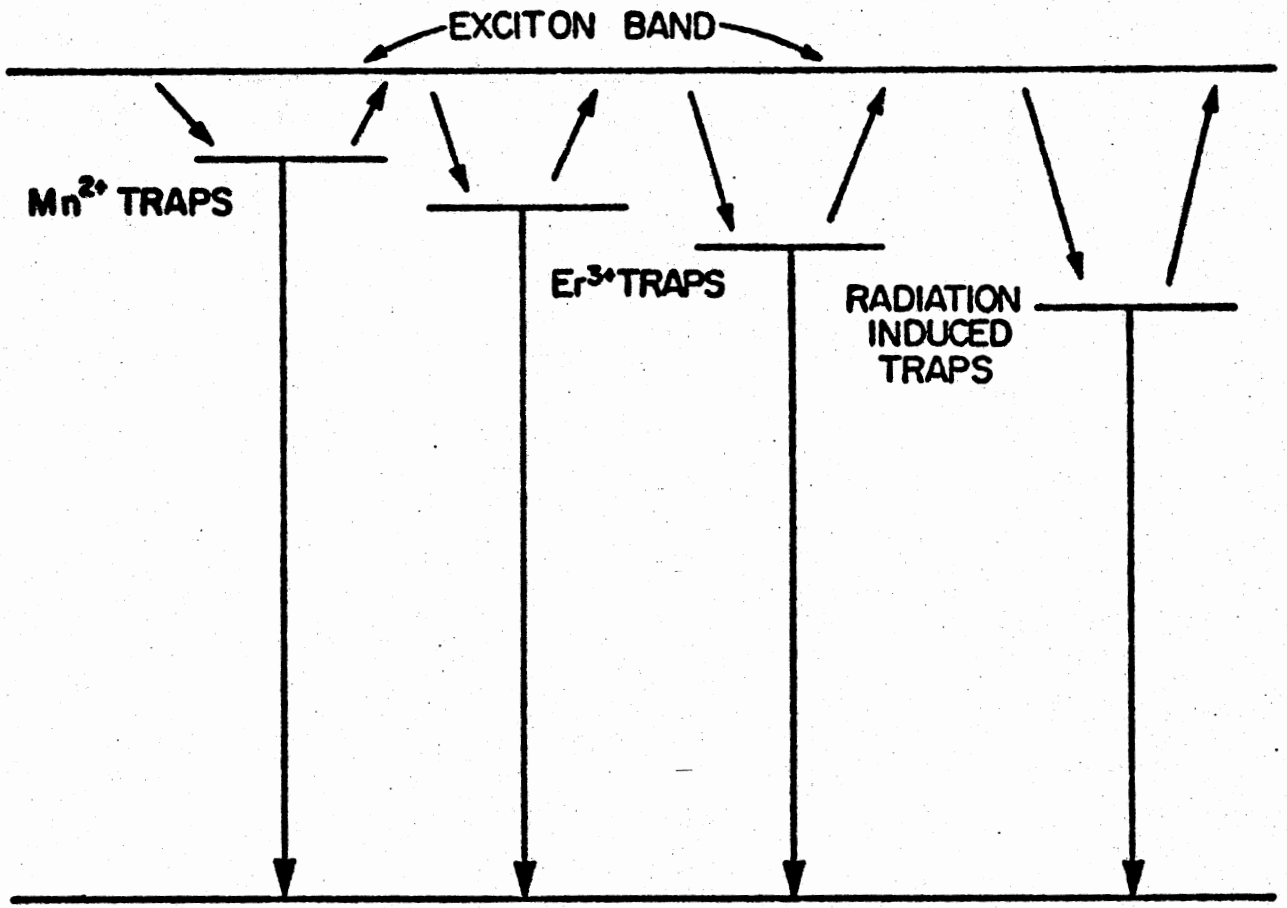

Figure 5. Trapping Model for Defect Perturbed Mn^{2+}

Electron-Phonon Interaction

Optical transitions between electronic states of single impurity ions are coupled to the vibrations of the lattice. This electron-phonon coupling causes the electronic states of certain ions to relax without the emission of radiation. Since these radiationless processes involve a combination of crystal field theory and lattice dynamics, an exact treatment still proves to be a formidible problem (69). Solid state theorists, however, over the years have developed approximate expressions useful in analyzing and predicting data about a particular type of impurity ion and/or host. Excellent reviews are found in the literature (70-73,64).

Early workers typically considered only the possibility of strong or weak electron-phonon coupling. Transition metals and radiation defects usually fit the strong coupling case; while, rare earths fit the case of weak coupling. Clearly, the rate of multiphonon emission is related to the distance between energy levels. For rare earths this rate follows an exponential gap law dependence (68,74-75). This rule may be rationalized as follows. The electron-phonon coupling that drives the nonradiative decay is proportional to the strain ε. The nonradiative rate can then be written for a n phonon process as

$$P_{nr} = C\varepsilon^{n} \tag{5}$$

where C is an arbitrary constant. Assume that the energy gap (ΔE) to the next lower level can be divided into n phonons of energy $\hbar\omega$. Then

$$P_{nr} = Ce^{\Delta E/\hbar\omega} \tag{6}$$

$$= Ce^{-(\Delta E/\hbar\omega|\ell n\varepsilon|)} \tag{7}$$

Thus the closer the energy levels, the higher the rate for nonradiative decay. From this rule fast nonradiative decay would be expected between the $^4F_{9/2}$ and $^4I_{11/2}$ levels of Er^{3+} shown in Figure 3. On the other hand, a very small nonradiative rate would be expected between the $^4I_{13/2}$ level and the ground state.

A number of different techniques closely related to experimental measurements have been developed (76-77) to determine multiphonon rates and to check this energy gap law. These techniques require either an absolute measurement or a calculation of the radiative rate. Recently, Struck and Fonger (53-57) have developed a Quantum Mechanical Single Configuration Coordinate Model. When absorption, emission, and lifetime data are available, a prediction of the temperature dependence of the nonradiative rate can be made from this model.

The QMSCC model of Struck and Fonger predicts the temperature quenching of the lifetime from the seven following experimentally related parameters: $\hbar\omega$ - the interacting phonon energy, P_U - the number of these phonons emitted over the energy gap of interest, T - temperature, a_{uv} - the relative offset of the two paraboli in the configuration coordinate curve, θ which is related to the ratio of the interacting phonon frequencies of the two levels u and v, and finally, N_{uv} and R_{uv} which are nonradiative and radiative electronic factors. A simplified flowchart to calculate these temperature quenchings of the lifetimes is described in the Appendix. The relationship of these parameters to the u and v parabolas is shown in Figure 6. Basically, P_U and θ are inserted into the following Mannebach recursion relations (53,80):

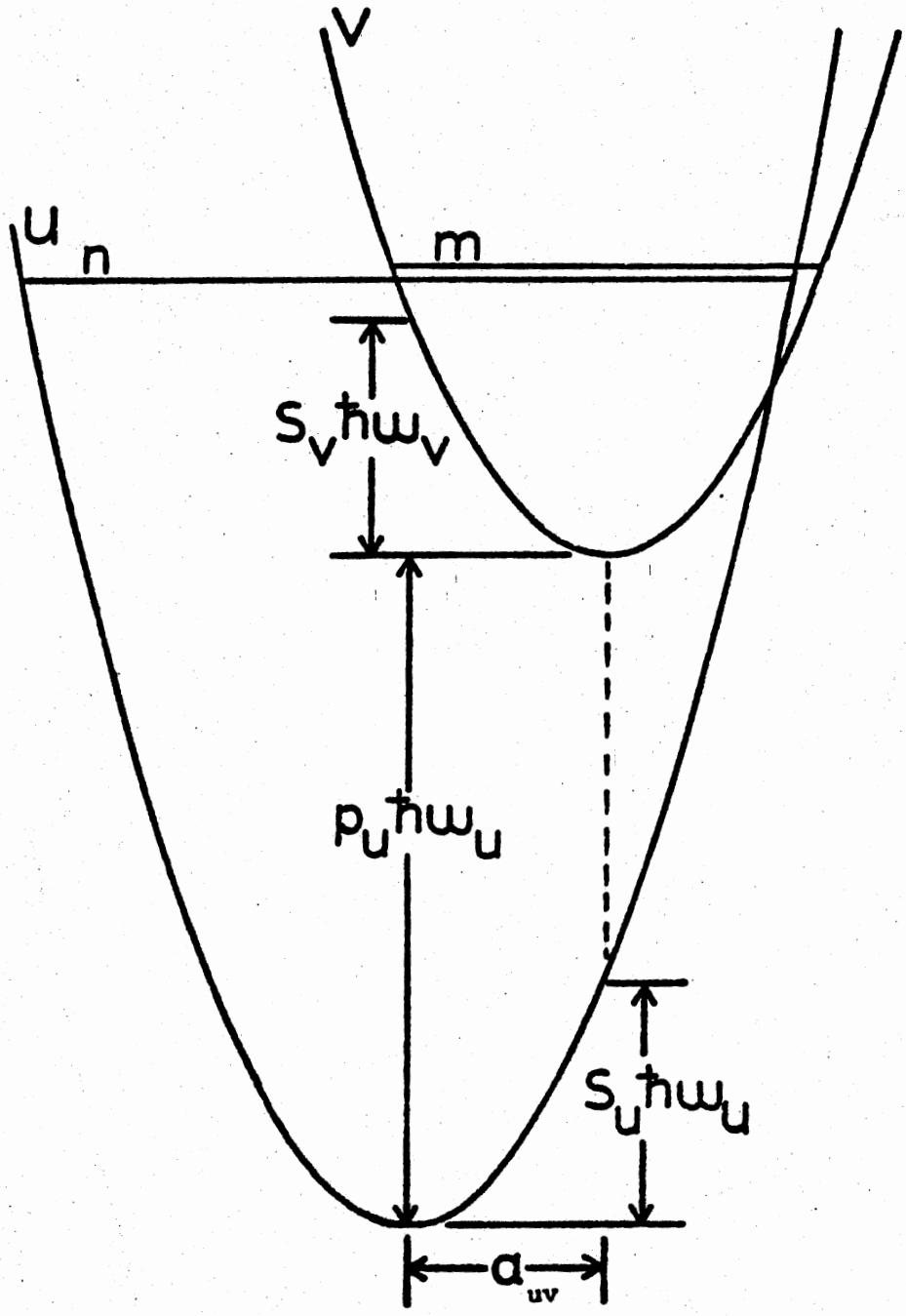

Figure 6. Struck and Fonger Radiationless Relaxation Model

$$(m+1)^{\frac{1}{2}}A_{n,m+1} = -m^{\frac{1}{2}}\cos 2\theta A_{n,m-1} - \frac{1}{2}a_{uv}\sin 2\theta\cos\theta\, A_{n,m} + n^{\frac{1}{2}}\sin 2\theta\, A_{n-1,m} \quad (8)$$

$$(n+1)^{\frac{1}{2}}A_{n+1,m} = n^{\frac{1}{2}}\cos 2\theta\, A_{n-1,m} + \frac{1}{2}a_{uv}\sin 2\theta\sin\theta\, A_{n,m} + m^{\frac{1}{2}}\sin 2\theta\, A_{n,m-1} \quad (9)$$

to calculate the overlap integrals ($\langle u_n | v_m \rangle$) of the nth harmonic oscillator wavefunction of the u parabola with respect to the mth harmonic oscillator wavefunction of the v parabola. The radiative and nonradiative rates ($R_{p_U v}$ and $N_{p_U v}$) are related to these overlap integrals through the U_{p_U} term in the following expression:

$$N_{p_U v} = N_{uv}U_{p_U} \qquad R_{p_U v} = R_{uv}U_{p_U} \quad (10)$$

which are partially governed by their respective energy balances for a v→u transition

$$h\nu_{zp,vu} - p_U\hbar\omega_u = 0 \qquad h\nu_{zp,vu} - p_U\hbar\omega_u + h\nu_{p_U} = 0. \quad (11)$$

Here $h\nu_{zp,vu}$ refers to the zero phonon energy while $h\nu_{p_U}$ refers to photon energy of all unresolved radiative transitions with quantum number p_U. These energy balances together with θ select particular overlap matrix elements for calculation of U_{p_U} in the following expression (53, eqns. 7 and 8)

$$U_{p_U} = \sum_{m=0}^{\infty}(1-r_v)r_v^m\left\{f_m\langle u_{p_U+i_m-1}|v\rangle_m^2 + (1-f_m)\langle u_{p_U+i_m}|v\rangle_m^2\right\} \quad (12)$$

for $p_U \geq 0$. Note first that the term outside the brackets predicts the temperature dependence of the rate through the Boltzmann factor ($r_v = \exp(-\hbar\omega_v/kT)$). The remaining undefined variables are as follows: i_m is the smallest integer $\geq (\hbar\omega_v/\hbar\omega_u)m$ and $f_m = i_m - \frac{\hbar\omega_v}{\hbar\omega_u} m = i_m - (\tan^2\theta)m$. Secondly note that for $\theta = 45^o$ ($\hbar\omega_v = \hbar\omega_u$), f_m is equal to zero. This means in the equal force constant case ($\theta = 45^o$)

$$U_{p_U}(45^o) = W_{p_U} = \sum_{m=0}^{\infty} (1-r_v) r_v^m \langle U_{p_U+m} | v_m \rangle^2 \quad \text{for } p_U \geq 0 \tag{13}$$

Thus for p_U equal to 14, the sum would start on the 14th row down with m=0 and then progressively down a diagonal from there (i.e. $\langle u_{15}|v_1\rangle^2$, $\langle u_{16}|v_2\rangle^2$ etc.). Using trial data in Equation 13, the square of these matrix elements and their sums reproduced the tables presented in references (53,55). For comparison with experimental measurements of the temperature dependence of the lifetime, the following expression can be used:

$$1/\tau = 1/\tau_o + N_{uv} U_{p_U} \tag{14}$$

where $R_{uv} = \frac{1}{\tau_o}$ is the low temperature radiative lifetime.

CHAPTER III

EXPERIMENTAL APPARATUS AND PROCEDURE

Sample Preparation

The $RbMnF_3$ and $RbMnF_3:Er^{3+}$ crystals were grown in the Oklahoma State University Crystal Growth Laboratory by means of modified Bridgeman and Stockbarger techniques (81-83). For $RbMnF_3:Er^{3+}$ the starting material consisted of RbF_2, MnF_2, and 1% ErF_3 in an Ultra Carbon (UT9 grade) crucible. This crucible was then placed in a vacuum system surrounded by a furnace with a spatial temperature gradient slightly above and below the melting point. This temperature gradient was produced by different densities in the platinum furnace windings. Actual crystal growth was achieved by moving the furnace so that the mixture first melts and then cools. A diagram of this apparatus is shown in Figure 7.

After crystal growth the sample was cut using an Imanco Macrotome diamond saw. Major irregularities were removed by hand by lapping on a dry abrasive manufactured by Buehler LTD. A Syntron LP-01 vibratory polisher with Linde Al distilled water slurry was used for fine polishing. The Er^{3+} concentration was found to be 500 ppm by optical absorption measurements of the $^4I_{13/2}$ band. Mass spectrometry indicated 3000 ppm. Both numbers are much less than the 1% Er^{3+} added to the melt.

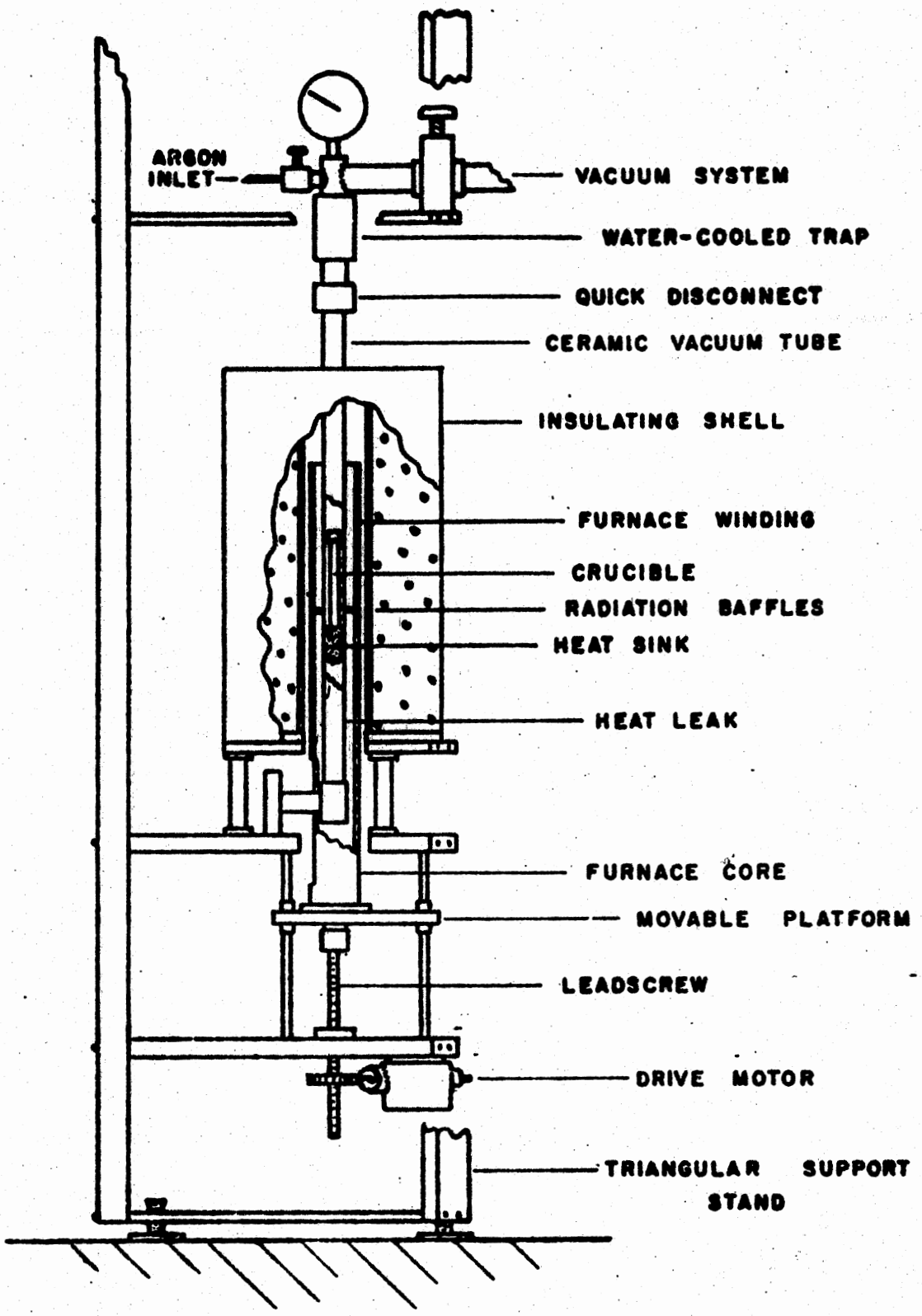

Figure 7. Oklahoma State University Bridgeman Apparatus

Optical Measurements

A Cary 14-S spectrophotometer was used to record optical density as a function of wavelength from three microns to 250 nm. The optical density, O.D. = $\log_{10}(I_o/I)$ is related to the absorption coefficient (α) by $\alpha = 2.303 \left(\frac{O.D.}{t}\right) cm^{-1}$ where t is the thickness of the sample. Several portions of the sample were measured with a micrometer to determine the thickness. A 0.1 O.D. slidewire, courtesy of J. Harmon, was used when greater sensitivity was needed. Low temperature measurements were made using a CTI cryogenerator or a Sulfrian cryostat. In the cryogenerator the temperature was controllable between 13K and 300K within $\pm$ 1K by the use of a resistance heater. The Sulfrian was controllable within $\pm$ 1K by the use of an immersion heater. In both cases a gold-iron versus chromel thermocouple allowed for easy measurement of temperature on a Keithley Model 160B Digital Multimeter. The cryogenerator thermocouple readings were checked with the expected values at liquid nitrogen, dry ice, ice, and room temperature.

For luminescence in the 250 nm to 900 nm region of the spectrum, the high resolution system shown in Figure 8 was used. Light from a xenon excitation source was passed through a Spex Minimate monochromator. To minimize stray light the unirradiated samples were excited parallel to the plane of the cold finger. The thinner irradiated samples were excited by light which made an angle of slightly more than 45^{o} with the face as shown in Figure 8. A rotatable tail section on the cryostat and cryogenerator allowed for easy signal to noise optimization.

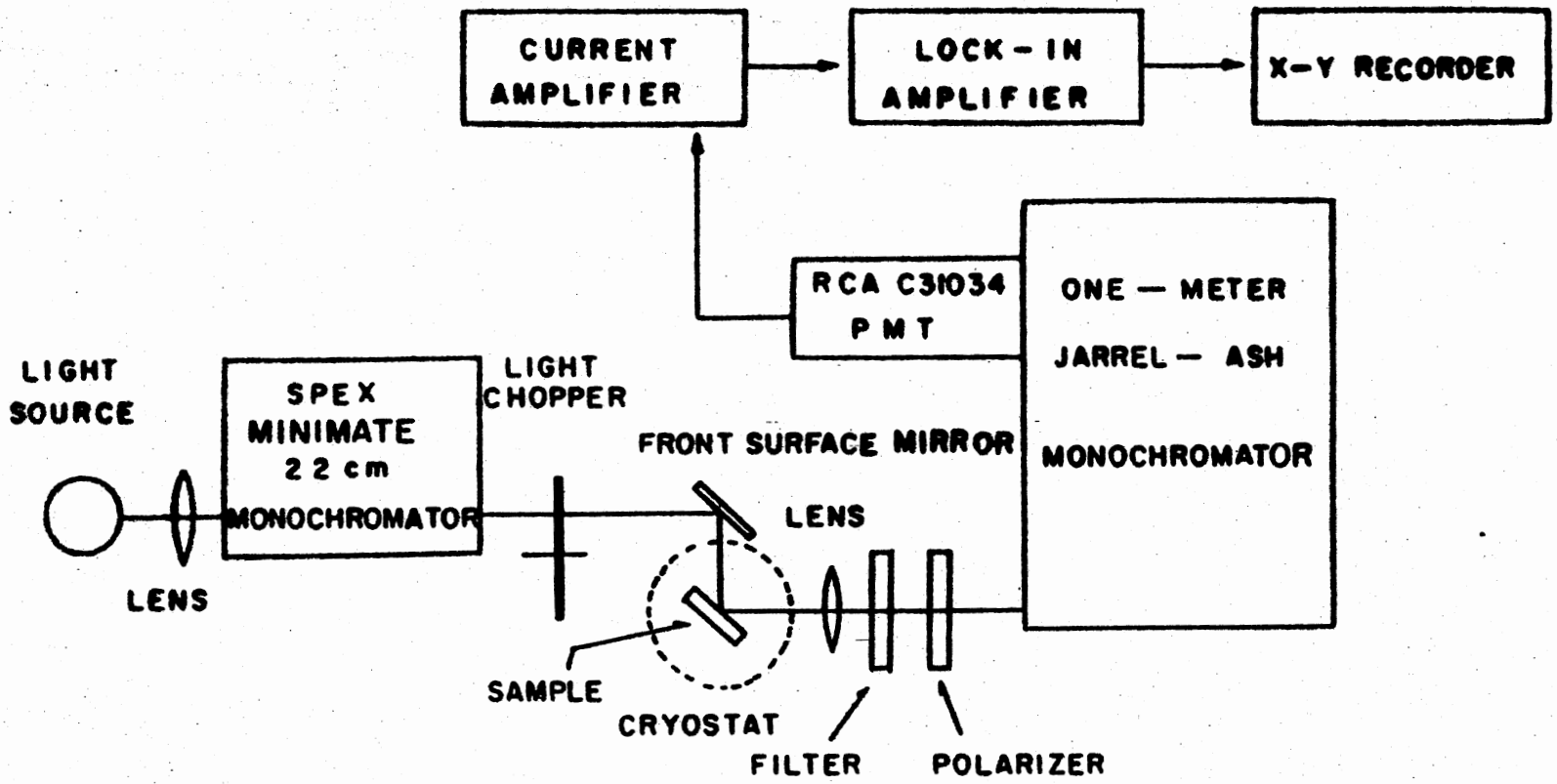

Figure 8. Block Diagram of High Resolution Visible Apparatus

Three quartz windows were used for optical excitation and detection, while an aluminum window was used for irradiating the sample. The emitted light was detected with a Jarrel-Ash one meter monochromator followed by an RCA 31034C photomultiplier tube. The photomultiplier tube was cooled to -20 C with a thermoelectric cooler manufactured by Products for Research Inc. A negative 1800 V.D.C. bias was provided by a John Fluke model 412A high voltage power supply. The output of the phototube was fed into a Keithley model 427 Current amplifier. A chopper placed before the sample enhanced the signal to noise for an emission band with a relatively short lifetime by providing a reference frequency for a Keithley model 840 Autoloc amplifier. The detected emission intensity can then be plotted versus wavelength on a Houston Instruments model 2000 Omnigraphic xy recorder. The measurement of an excitation spectrum consisted of setting the Jarrel-Ash emission monochromator to a particular emission peak and then varying the wavelength of the Spex exciting monochromator. For the $^4F_{9/2} \rightarrow {}^4I_{15/2}$, $^4I_{9/2} \rightarrow {}^4I_{15/2}$, and $^4I_{13/2} \rightarrow {}^4I_{15/2}$ transitions of Er^{3+}, the following filters were used: Corning CS3-69, Corning CS2-64 sharp cutoff, and a Corning CS7-57. The detection system was calibrated from a G.E. QL-157 quartz iodine standard lamp traceable to the National Bureau of Standards.

A second lower resolution system was used to detect emission from 250 nm to 2 microns. A block diagram of this system is illustrated in Figure 9. In this system a 300W xenon lamp was shone through another Spex Minimate. The emission was analyzed with a .5 meter Bausch and Lomb monochromator to either an RCA 7102 Photomultiplier

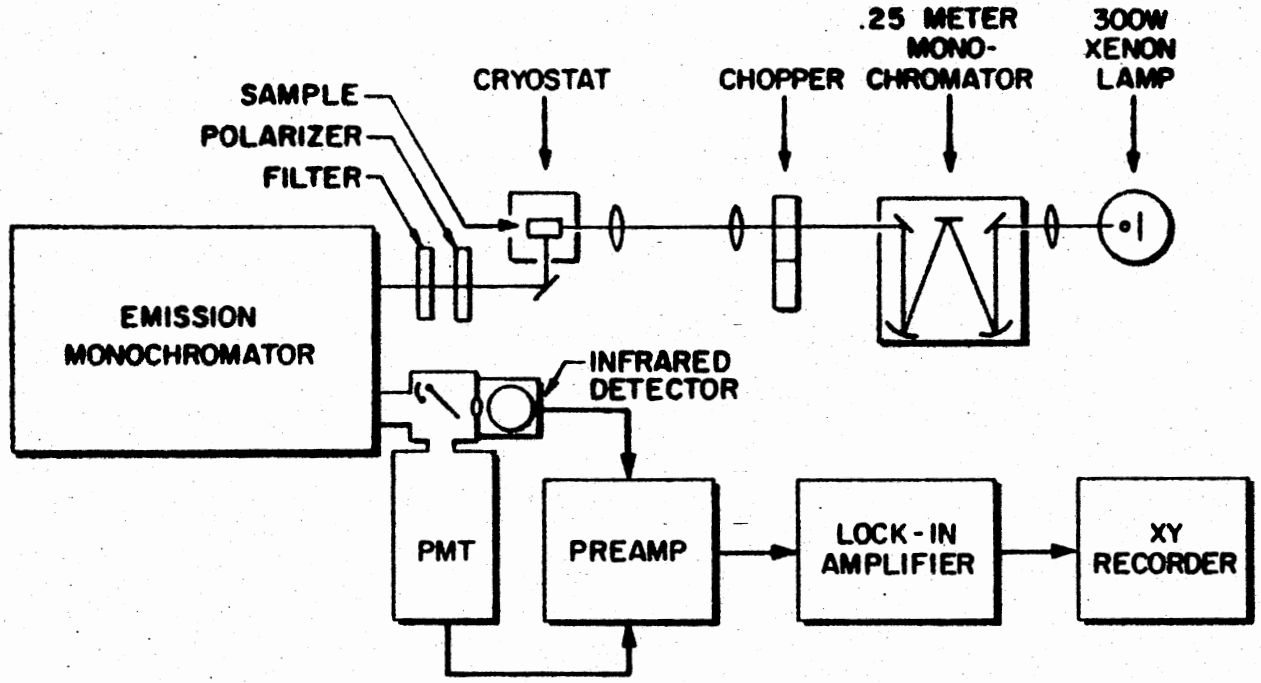

Figure 9. Block Diagram of Visible and Infrared Luminescence Apparatus

tube in dry ice or an Optoelectronics OTC 22-53XX two stage thermoelectrically cooled PbS cell. The electronics for this photoconductive detector are summarized in Figure 10. A Keithley model 103A Nanovolt amplifier was used as a preamplifier for the PbS detector. In this detection system the chopper may be placed after the emission monochromator. In order to reduce blackbody radiation from the chopper blade to the detector, a Corning CS 0-51 filter was used. This problem was eliminated for future studies by a small Math Associates Frequency Programable light chopper before the emission monochromator.

A block diagram of the lifetime measurement system is shown in Figure 11. The exciting source is a General Radio model 1538 Strobatac with a 5μ second pulse width. Particular excitation wavelength regions were selected with a filter. The electronic response of the normal preamplifiers was either correctable or sufficiently fast. The Nicolet 1070 Signal Averaging System has its own internal time base which determined the rate at which the intensity was stored in the memory locations after the trigger from the strobe. In addition this instrument digitally added a number of sweeps to improve the signal to noise ratio. The digitally stored data then slowly transmitted to an xy recorder. It should also be noted that the PbS cell must be raised to room temperature to reduce the intrinsic detector response time.

Experimental Procedure

It was mentioned earlier that a chopper before the sample enhanced those emission bands with short lifetimes. From this it is clear that emission bands with long lifetimes can be effectively eliminated

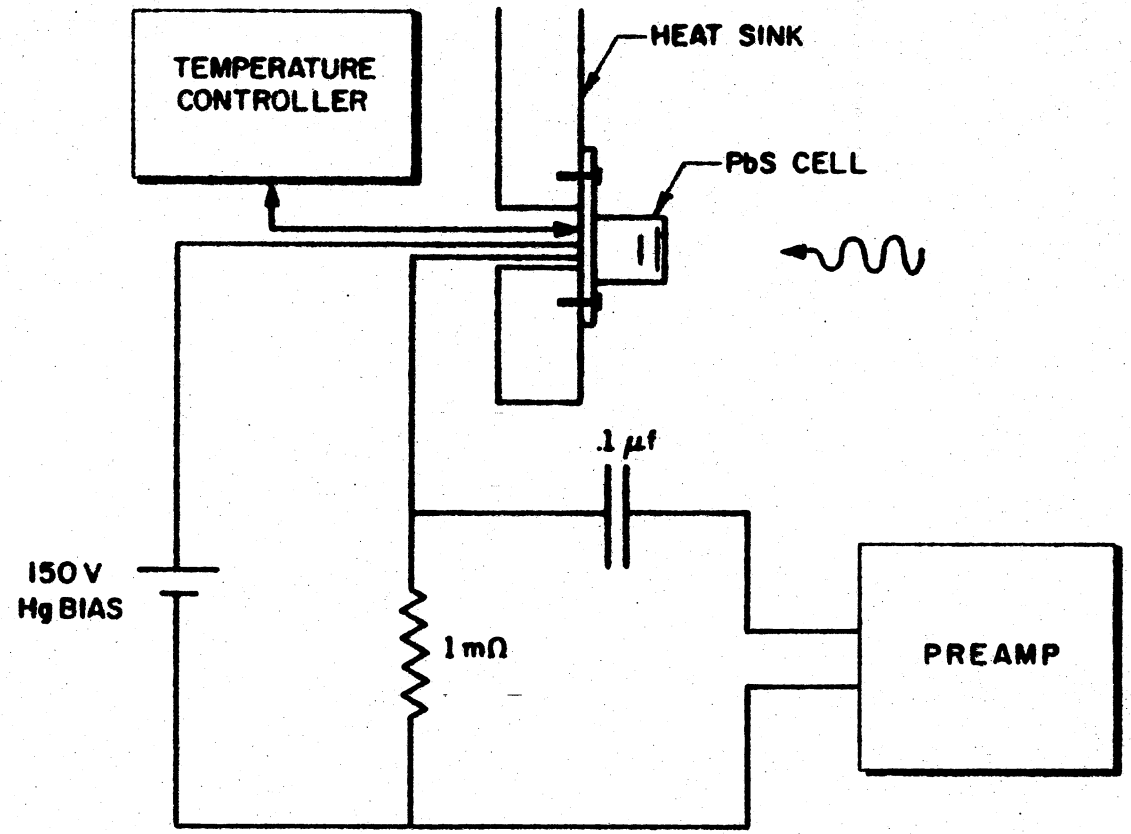

Figure 10. Electronics for PbS Detection

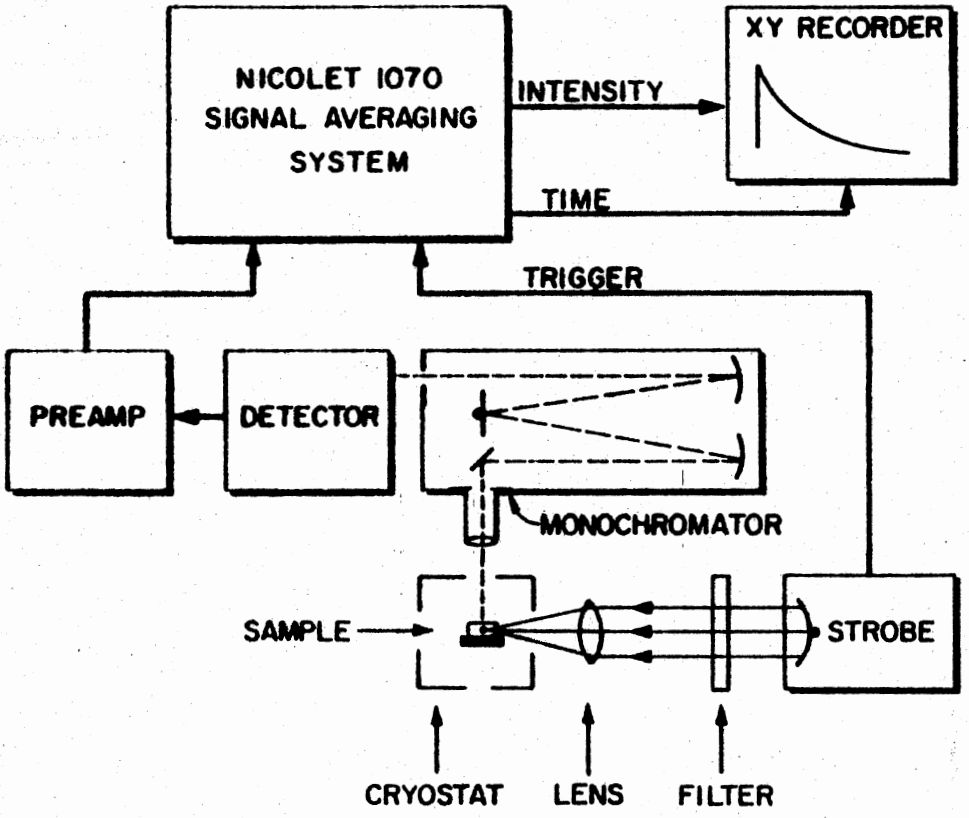

Figure 11. Block Diagram of Lifetime Detection System

through the use of a chopper of an appropriate frequency. This idea was experimentally important for $^4F_{9/2}$ Er^{3+} emission which rides on top of the tail of the long lifetime Mn^{2+} emission.

The $RbMnF_3:Er^{3+}$ samples subjected to electron irradiation were irradiated with 1.7 M.e.V. electrons for 30 minutes. The sample was placed 15 cm from the accelerator, and a current of 8μ was used. The room temperature sample was enclosed in aluminum foil and attached to the aluminum block. In addition, sample heating during the irradiation was avoided by irradiating in two minute intervals separated by two minutes of no irradiation.

CHAPTER IV

RESULTS

Unirradiated $RbMnF_3:Er^{3+}$

The energy levels for Mn^{2+} and Er^{3+} ions in $RbMnF_3$ are illustrated schematically in Figure 3. The notation for the various energy levels is discussed in Chapter II. Actual positions of the Mn^{2+} bands were taken from the low temperature optical absorption spectrum shown in Figure 12. The peak positions are summarized in Table I. It should be noted that, in addition to the strong Mn^{2+} absorption bands, weaker Er^{3+} absorption bands are also observed. Emission can occur from either of the two Mn^{2+} defect-perturbed levels shown in Figure 3 (traditionally labeled 5820 Å and 6300 Å) or from the Er^{3+} levels.

Manganese Emission

At very low temperatures only intrinsic Mn^{2+} emission occurs in $RbMnF_3$, but by 5K the observed 582 nm (5820 Å in Figure 3) band is present due to energy transfer to impurity perturbed Mn^{2+} ions and subsequent emission from these sites (39,40). As the temperature is increased to above 40K, energy transfer occurs from these sites to different defect-perturbed Mn^{2+} ions which have shorter lifetimes. This luminescence occurs at 630 nm (6300 Å in Figure 3). The 630 nm

TABLE I

POSITIONS OF Mn^{2+} AND Er^{3+} ABSORPTION PEAKS AT 13K IN $RbMnF_3:Er^{3+}$

Mn^{2+}		Er^{3+}	
Level	Energy (cm^{-1})	Level	Energy (cm^{-1})
$^4A_{2g}$	38,240.9		
$^4T_{1g}$	32,959.9 32,626.4 32,478	$^4G_{11/2}$	26,759 26,652 26,367 26,212
$^4T_{2g}$	28,498.1 28,312 28,232.6 28,011.2	$^4F_{9/2}$	15,500
^4E_g	25,994 25,879 25,682 25,396.8 25,236	$^4I_{11/12}$	10,511
$^4A_{1g}$	25,138		
$^4T_{1g}$	23,329 23,095 22,321 19,230.7 19,094 18,722 18,628.9 18,395 18,292	$^4I_{13/2}$	6596.3 6574.62 6563. 4 6560 6544.5 6524* 6513.8 6504

*Strongest.

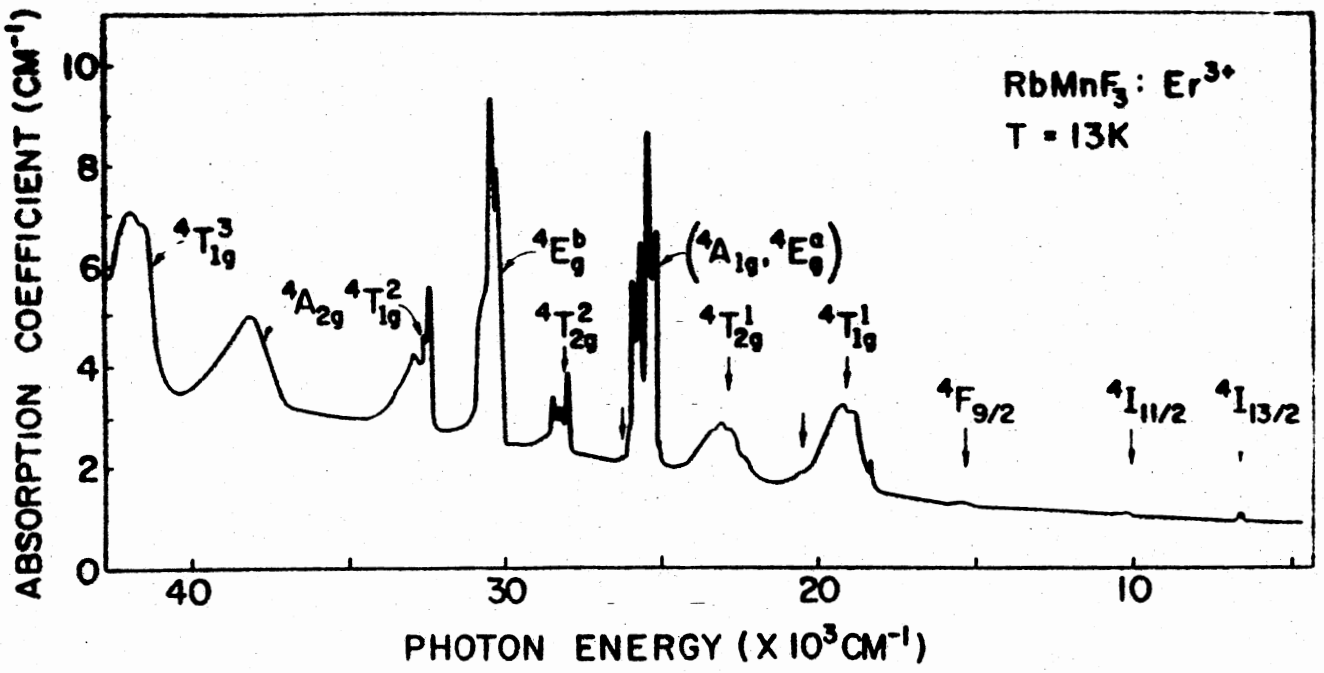

Figure 12. Low Temperature Optical Absorption Spectrum for $RbMnF_3:Er^{3+}$

band decreases in intensity until no emission is detectable above 120K. These results are portrayed in Figure 13 and 14 for both undoped $RbMnF_3$ and $RbMnF_3:Er^{3+}$. The presence of the larger Er^{3+} ion in the lattice obviously causes some perturbation just as does the addition of the smaller Mg^{2+} for Mn^{2+} (41). Moreover, in the case of erbium doping there is need for charge compensation such as a positive ion vacancy for each Er^{3+} ion. The error bars shown in Figure 14 for the lifetime measurements of the 630 nm bands are large because of the much greater intensity and longer lifetimes of the 582 nm band at temperatures below 40K. Above this temperature, of course, the 582 nm band has disappeared and the error bars are much less.

The data shown in Figures 13 and 14 are similar to the previously published results of Holloway et al. (36) and Gooen et al. (40) for undoped material. The minor difference between the data presented here and that of Gooen et al. (40) for the temperature dependence of the lifetime for the 582 nm emission is most likely due to sample variation rather than to measurement error (41). The temperature dependence of the lifetime of the 582 nm emission can be fit with an "activation type" expression of the form

$$\frac{1}{\tau} = \frac{1}{\tau_o} + \frac{1}{\tau_{NR}} e^{-\Delta/kT} \qquad (15)$$

In this case τ_{NR} is the nonradiative lifetime, Δ is an activation energy, and τ_o is assumed to be the radiative lifetime. A summary of these parameters is given in Table II together with those from other crystal systems (41,45,84,85).

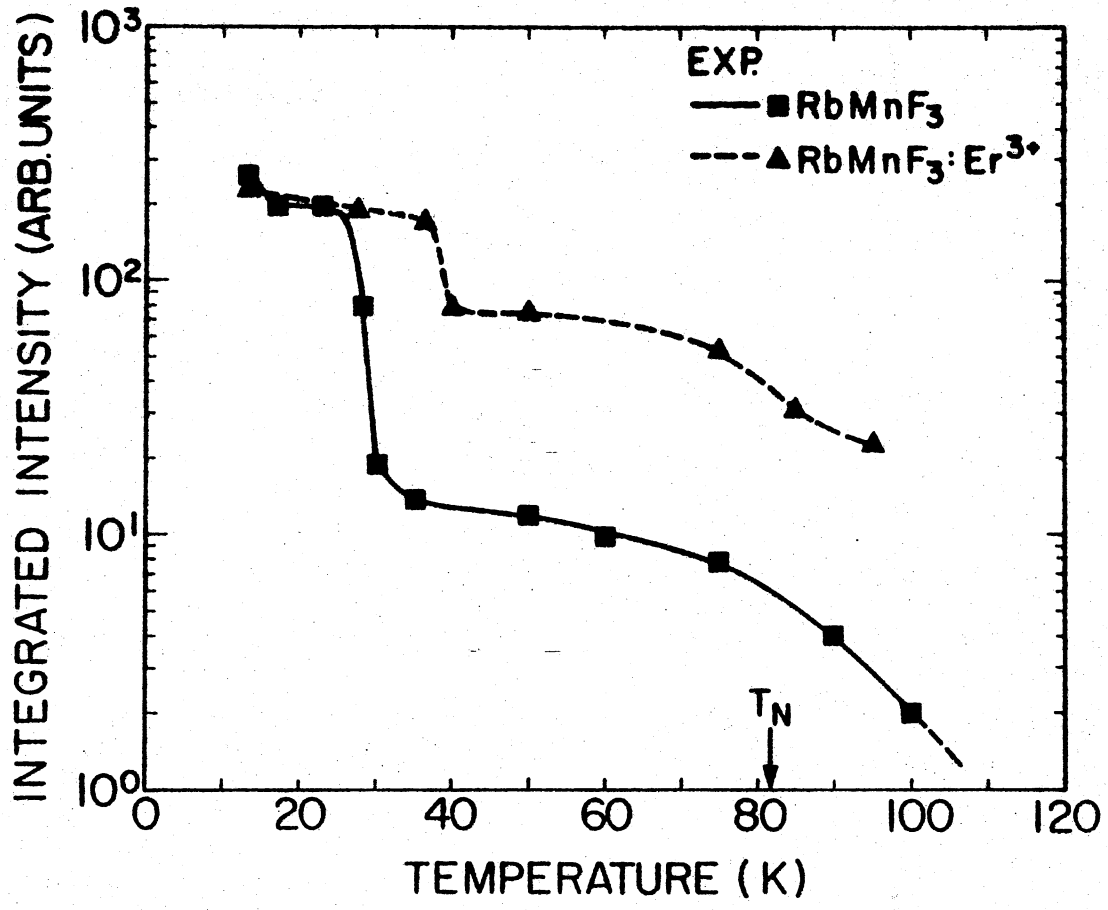

Figure 13. A Comparison of the Temperature Dependence of the Mn^{2+} Integrated Intensities for $RbMnF_3$ and $RbMnF_3:Er^{3+}$

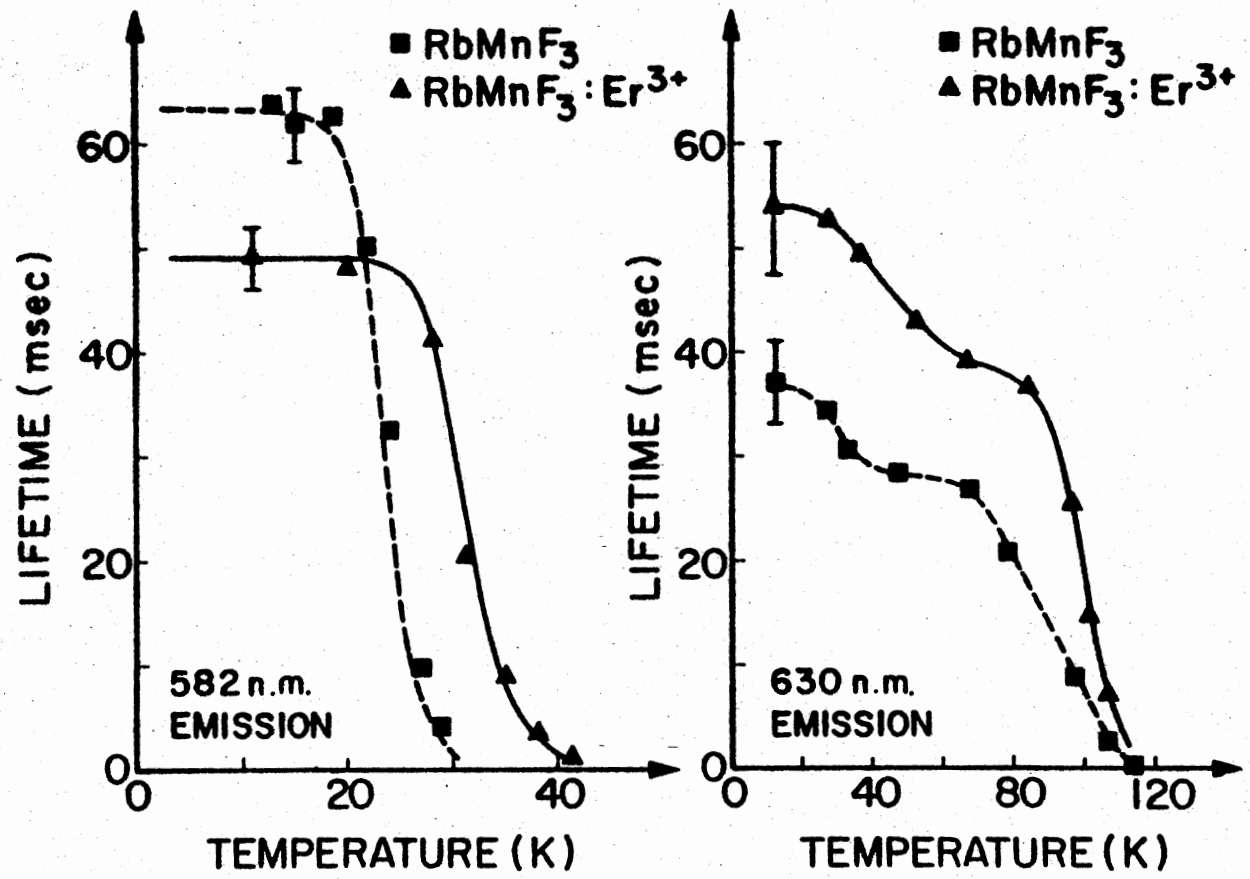

Figure 14. A Comparison of the Temperature Dependence of the Lifetime for the 582 nm and 630 nm Emissions in Undoped $RbMnF_3$ and $RbMnF_3:Er^{3+}$

TABLE II

LIFETIME FITTING PARAMETERS FOR THE TEMPERATURE DEPENDENCE OF THE IMPURITY PERTURBED Mn^{2+} EMISSION IN SIMILAR CRYSTALS

Material	τ_o(msec)	τ_{NR}(msec)	$\Delta(cm^{-1})$
$RbMnF_3$	63	4×10^{-5}	227
$RbMnF_3$ (40)	5	10^{-6}	300
$RbMnF_3:Er^{3+}$	49	1.68×10^{-6}	320
MnF_2 (45)	38	2.5×10^{-5}	250
$MnF_2:Er^{3+}$ (45)	34	10^{-3}	250
$KMnF_3$ (84,85)	60	-----	---
$RbMn_xMn_{1-x}F_3$ (41) $x=.3$	47	10^{-3}	285
$RbMg_xMn_{1-x}F_3$ (41) $x=.6$	33	5×10^{-3}	304

Several peripheral experimental observations may be of interest. The sharp line structure on the high energy side of the 630 nm band for both the doped and undoped material is different than that for the 582 nm emission. There are differences also between the doped and undoped specimens in the sharp line sequences. It was observed that the intensity of the Mn^{2+} emission takes a time τ_{max} to reach a maximum before decaying and for the temperature range of 25- 30K our observations agreed with those reported by Gooen et al. (40).

Er^{3+} Emission

The low temperature emission spectrum for $RbMnF_3:Er^{3+}$ is shown in Figure 15. The intense emission in the 582 nm or 17,182 cm^{-1} region of the spectrum is due to Mn^{2+}. The sharp lines are mostly impurity perturbed zero phonon lines (39). On the low energy side of the Mn^{2+} emission, near 15,000 cm^{-1}, the $^4F_{9/2} \rightarrow {}^4I_{15/2}$ emission for Er^{3+} is shown. The groups of lines in the 9813 cm^{-1} and 6464 cm^{-1} regions are transitions from the $^4I_{11/2}$ and $^4I_{13/2}$ levels of Er^{3+} to the ground state. Henceforth, these Er^{3+} transitions under the arrows in Figure 15 will be referred to by the level from which they originate.

In Figure 16 an expanded view of $^4F_{9/2}$ and $^4I_{11/2}$ luminescence is shown. Since the Mn^{2+} lifetime is very long at low temperatures, the Mn^{2+} background was subtracted from the $^4F_{9/2}$ emission by placing a 450 hz chopper in the exciting light. Integration of the emission intensity of Er^{3+} results in a plot of the temperature dependence of the intensity as shown in Figure 17. The rise in Er^{3+} intensity occurs in the same temperature region that the Mn^{2+} intensity decreases. This

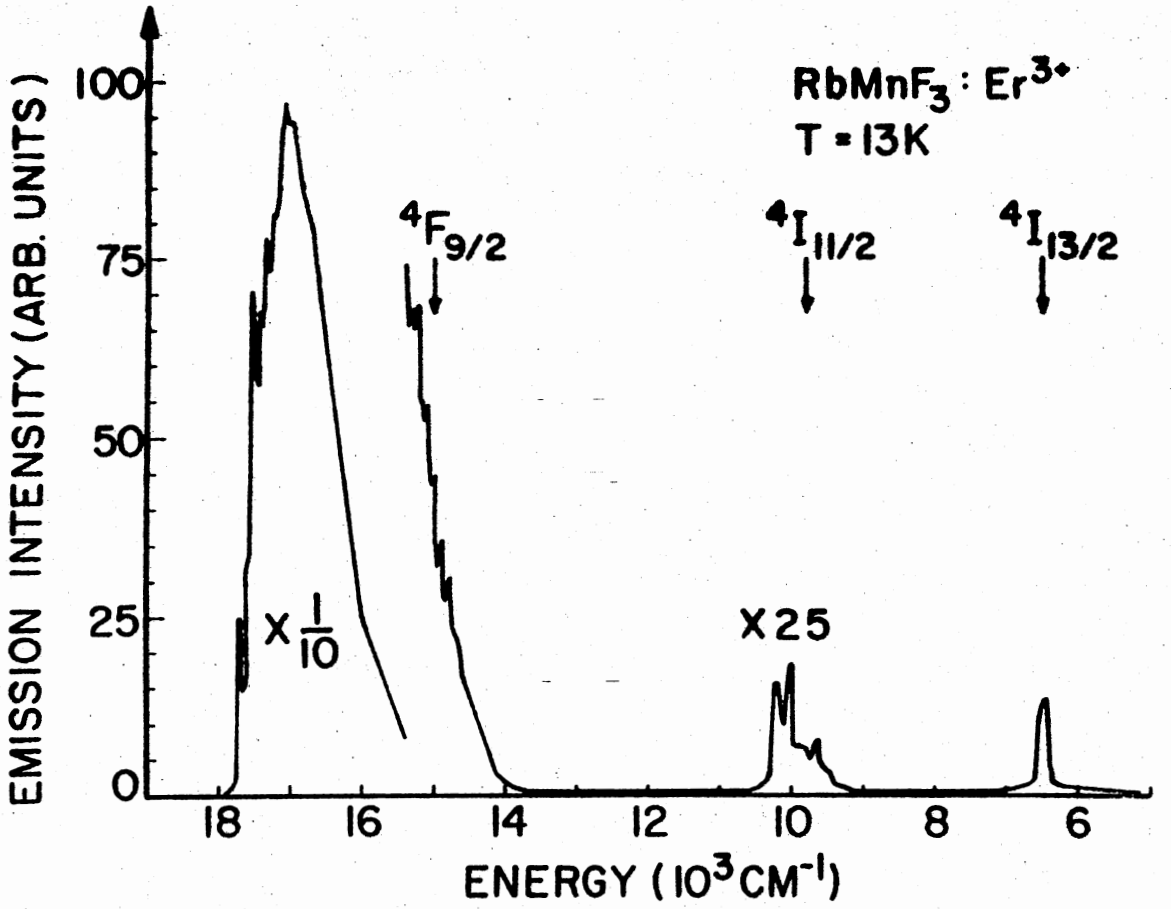

Figure 15. Low Temperature Emission Spectrum for $RbMnF_3:Er^{3+}$

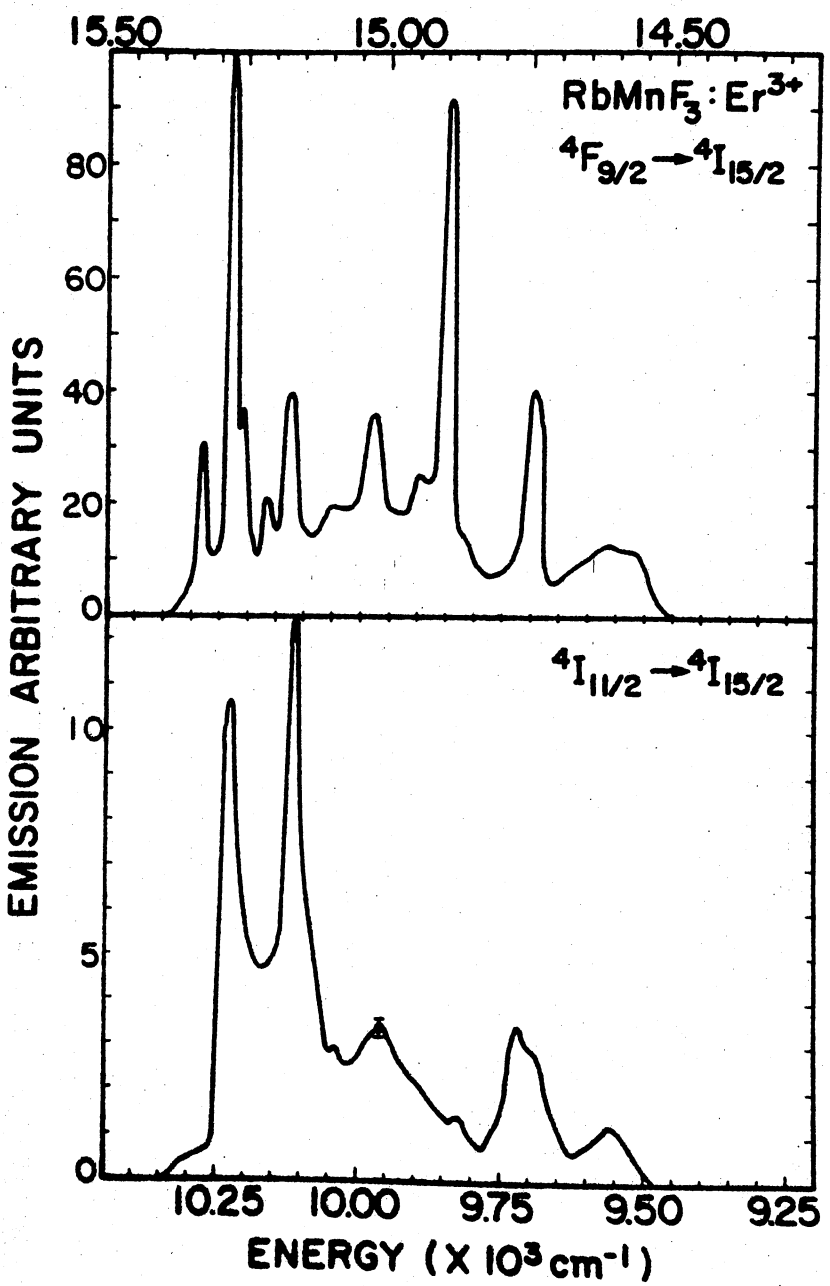

Figure 16. An Expanded View of the $^4F_{9/2}$ and $^4I_{11/12}$ Emissions in $RbMnF_3:Er^{3+}$

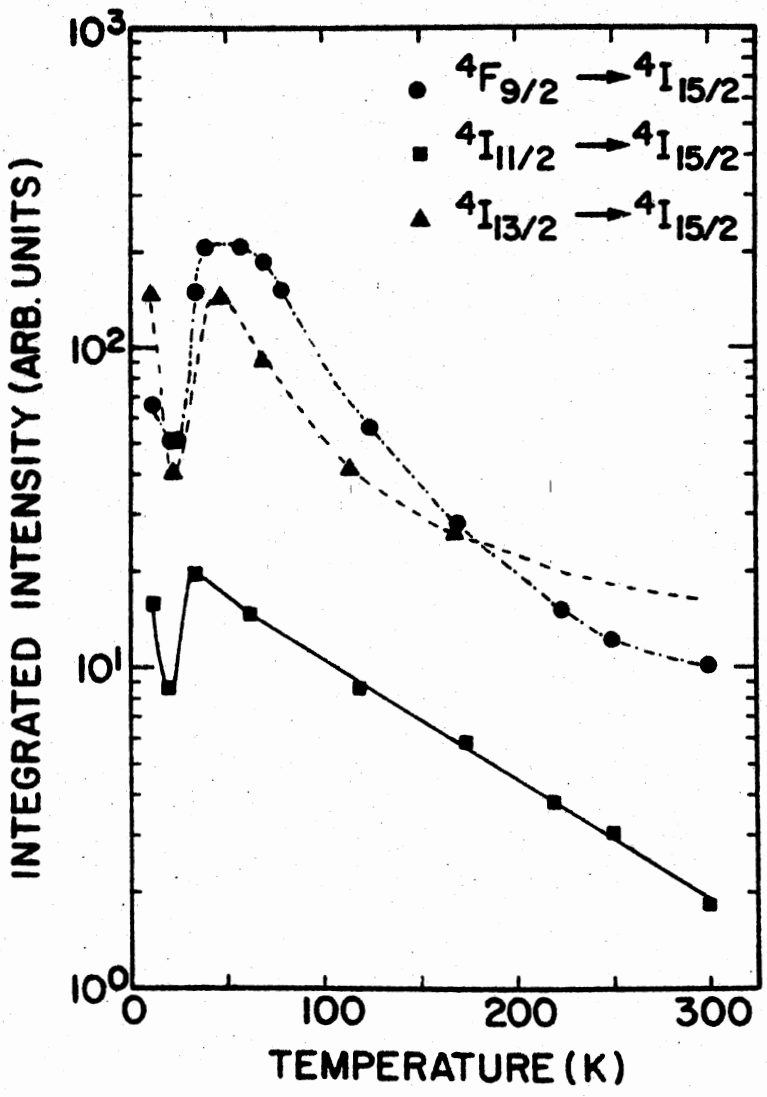

Figure 17. A Temperature Dependence of the Integrated Intensity for Each of the Observed Er^{3+} Transitions

This suggests energy transfer from $Mn^{2+} \rightarrow Er^{3+}$. For each of the three Er^{3+} transitions shown, a different detector was used to obtain the integrated intensity. An estimate of the relative intensities was made by comparing the $^4F_{9/22}$ to $^4I_{11/12}$ emissions using RCA7102 photomultiplier tube and the $^4I_{11/12}$ to $^4I_{13/2}$ emissions using a PbS cell. The relative intensities may be different ($\pm$ 50%) because of interferring Mn^{2+} emission and the temperature dependence of the lifetime.

In Figure 18 low temperature excitation spectrum is shown for Mn^{2+} and the $^4F_{9/2}$ Er^{3+} emissions (see Figure 15). The similarity of the manganese excitation spectrum (dashed line) with the Er^{3+} excitation spectrum (solid line) indicates that there is $Mn^{2+} \rightarrow Er^{3+}$ energy transfer. In addition to the broad Mn^{2+} excitation bands, several sharp lines are observed. These are due to direct excitation of the erbium. As the temperature is raised to 40K, the excitation bands due to Mn^{2+} increase in intensity; while, the $^4F_{9/2}$ Er^{3+} excitation band remains relatively constant. As the temperature is increased to 300K the manganese bands decrease in intensity but are still clearly distinguishable. Similar behavior was found for the $^4I_{11/2}$ and $^4I_{13/2}$ Er^{3+} emissions.

From the overlap of the Mn^{2+} emission with the $^4F_{9/2}$ band shown in Figure 15, it is clear that any attempt to measure the lifetime of the $^4F_{9/2}$ should be a sum of at least two exponentials. Fortunately, below 120K the Mn^{2+} emission has a much longer lifetime than $^4F_{9/2}$. This allows for an easy separation. Above 140K, the Mn^{2+} emission intensity and lifetime have decreased sufficiently to be no longer a problem. A single exponential decay was found for the

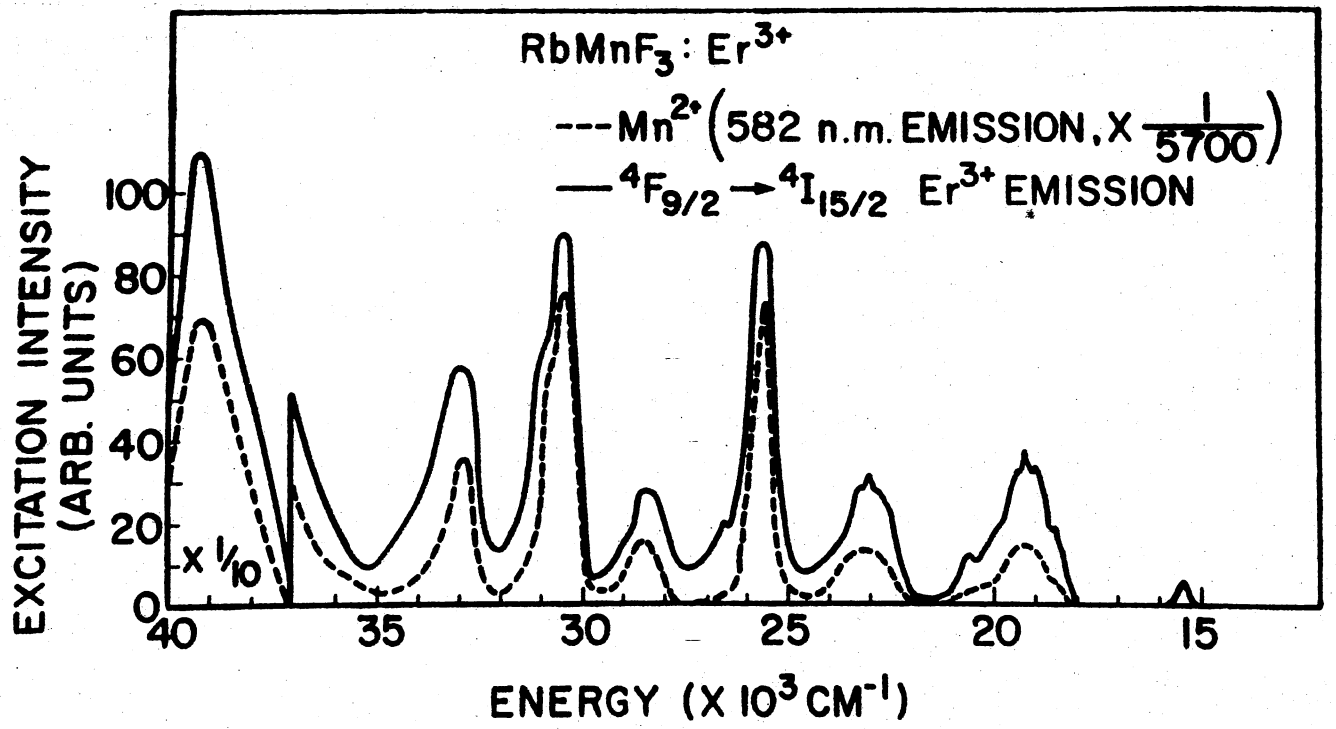

Figure 18. An Excitation Spectrum for the $^4F_{9/2}$ Emission Shown in Figure 16

$^4F_{9/2}$ portion of the total decay. The temperature dependence of the lifetimes for the three Er^{3+} luminescence transitions are depicted in Figure 19.

As can be seen from Figure 3, energy transfer from Mn^{2+} ions can populate the $^4F_{9/2}$ level of Er^{3+} resulting in emission. It is clear also that nonradiative transitions from $^4F_{9/2}$ to $^4I_{9/2}$ and subsequently to $^4I_{11/2}$ and $^4I_{13/2}$ take place. This means that both the $^4I_{11/2}$ and $^4I_{13/2}$ emissions can increase in intensity as a function of time before decaying because of the nonradiative transitions from the upper levels. This type of decay is often called "fluorescent rise type" of decay (46). A fluorescent rise type of decay was not observed for the $^4I_{11/2}$ emission on the time scales used to measure the single exponential decay. However, the $^4I_{13/2}$ emission was found to be the fluorescent rise type of decay. As the temperature increased, the time (t_{max}) to reach the maximum intensity decreased. This behavior of the $^4I_{13/2}$ emission is illustrated in Figure 20.

Irradiated $RbMnF_3:Er^{3+}$

When $RbMnF_3:Er^{3+}$ was irradiated for thirty minutes with 1.7 M.e.V. electrons at 300K, two additional defect emission bands were observed at 710 nm and 790 nm. These two bands are seen in the low temperature spectra shown in Figure 21. These spectra were taken with unchopped light. The relative intensities of the 710 nm band versus the 790 nm band change with temperature. When chopped light was used to excite the sample, contributions from the 790 band were eliminated. Thus, it is

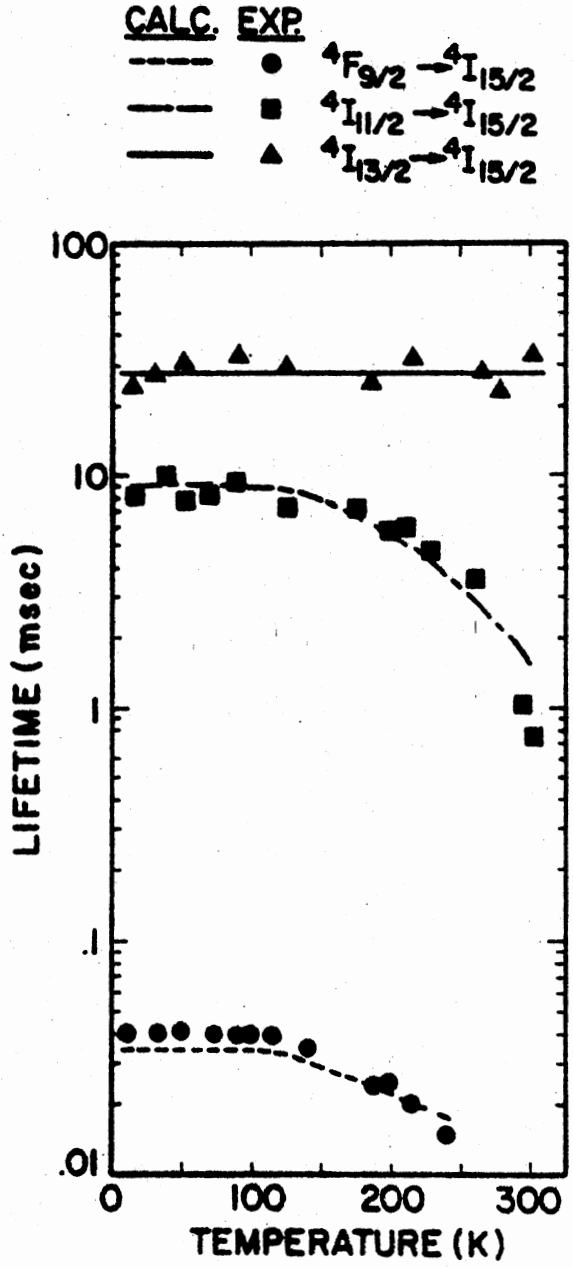

Figure 19. Temperature Dependence of the Lifetime for Each of the Er^{3+} Emissions

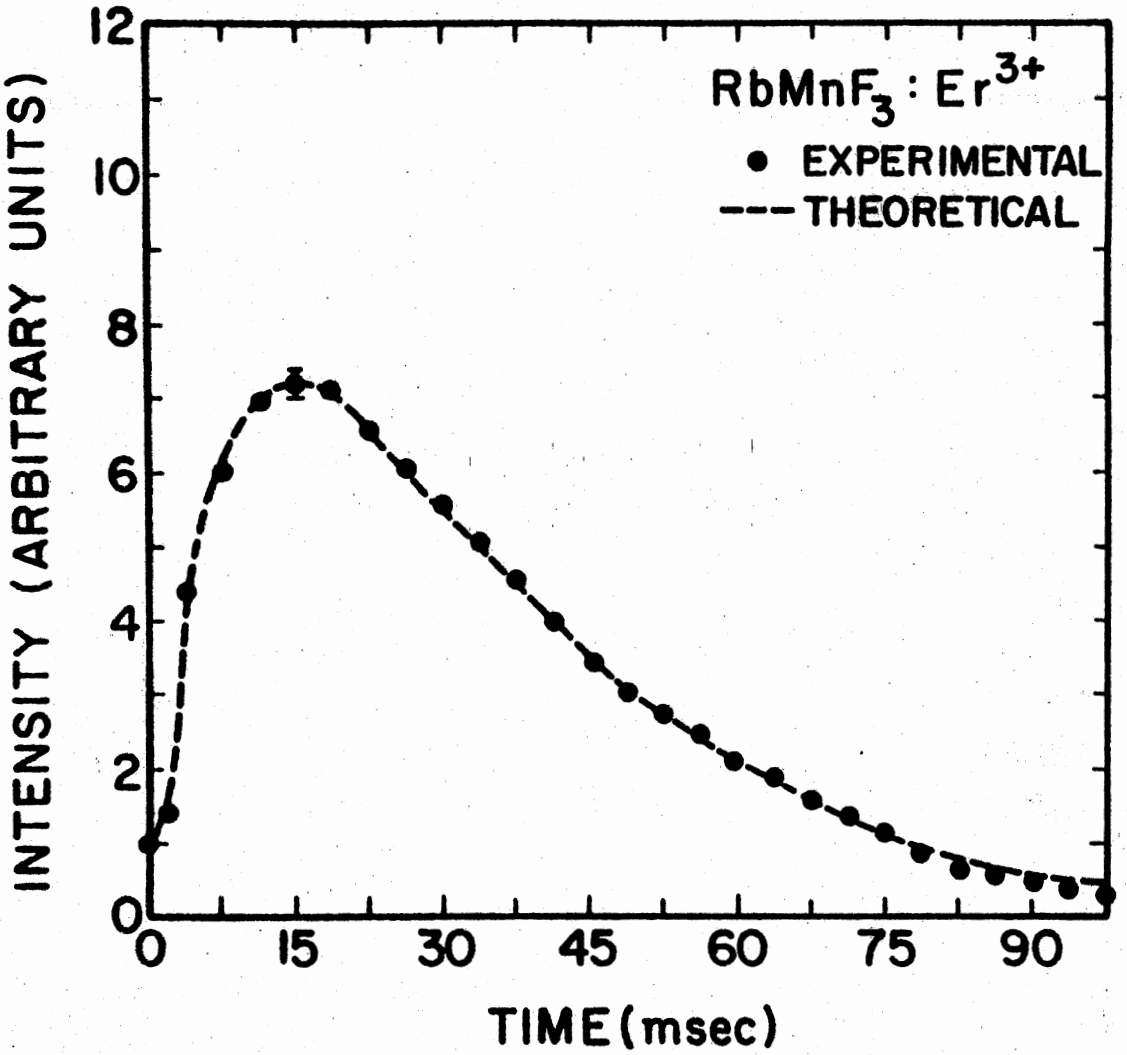

Figure 20. The Emission Intensity from the $^4I_{13/2}$ Level of Er^{3+} in $RbMnF_3$ at 33K as a Function of Time; The Experimental Points are Fit with a Dashed Theoretical Line

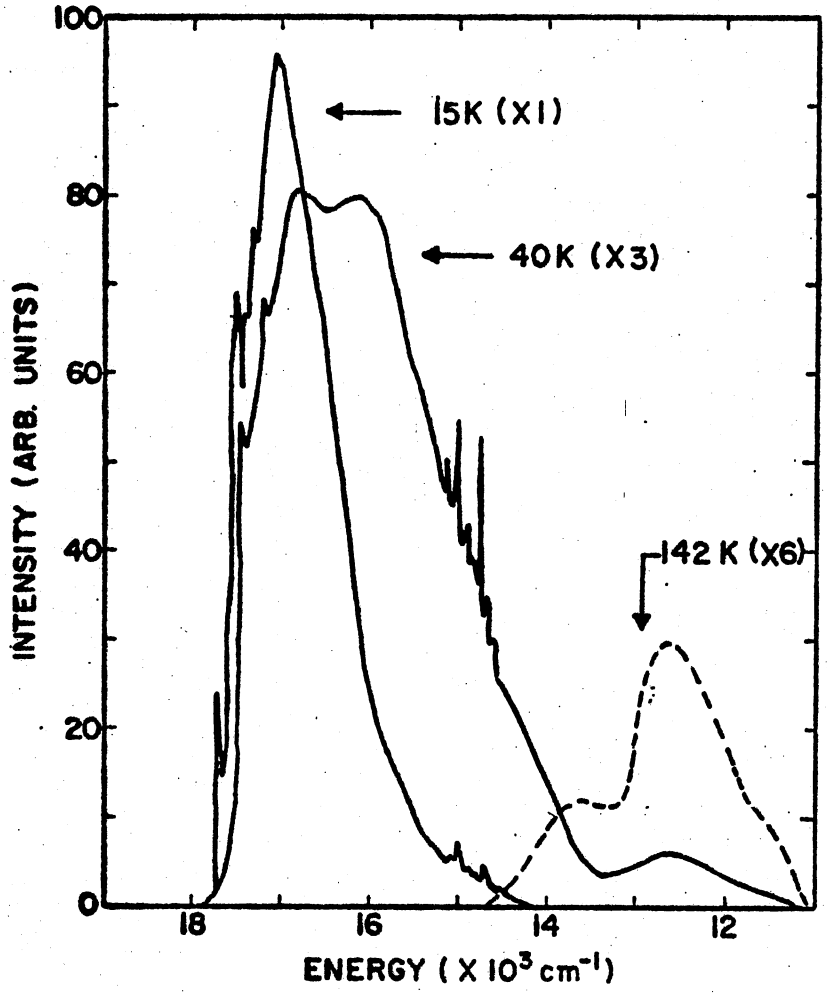

Figure 21. Low Temperature Emission Spectra for $RbMnF_3:^{3+}$ Which has been Irradiated for 30 Minutes with 1.7 M.e.V. Electrons at 300K

possible to compare the temperature dependence of the integrated intensity for the 710 nm and 790 nm emissions. These two emission bands are compared with the $^4F_{9/2}$ Er^{3+} emission and the impurity perturbed Mn^{2+} emission in Figure 22. The scale for each of these integrated intensities is related.

Additional differences between the 710 nm and 790 nm emissions can be seen in excitation and lifetime measurements. The excitation spectra for the 710 nm and 790 nm emission bands at 140K are respectively shown in Figures 23 and 24. The low temperature 582 nm Mn^{2+} excitation spectrum has been included in these figures for comparison. The 790 nm excitation spectrum follows the excitation spectrum of the 630 nm Mn^{2+} band below 18,000 cm^{-1}. The 710 nm excitation spectrum has relative intensities and a different spectral shape on the low energy side of Figure 23. The peaks at 17,500 cm^{-1} and 23,300 cm^{-1} are due to direct excitation of radiation-perturbed manganese ions. Other bands mirroring the 630 nm manganese excitation spectrum are due to energy transfer from the manganese to radiation-perturbed manganese ions. These energy transfer excitation bands are not present when the temperature is changed from 147K to 13K. The lifetime of the 710 nm emission is sufficiently short and could not be measured on our apparatus. The temperature dependence of the lifetime for the 790 nm emission is shown in Figure 25.

Since there exists the possibility that electron irradiation produced defects can perturb the Er^{3+} ions, an emission spectrum for the $^4F_{9/2}$ Er^{3+} emission was taken. This is shown in Figure 26. The bands are in the same position and about the same relative intensities as

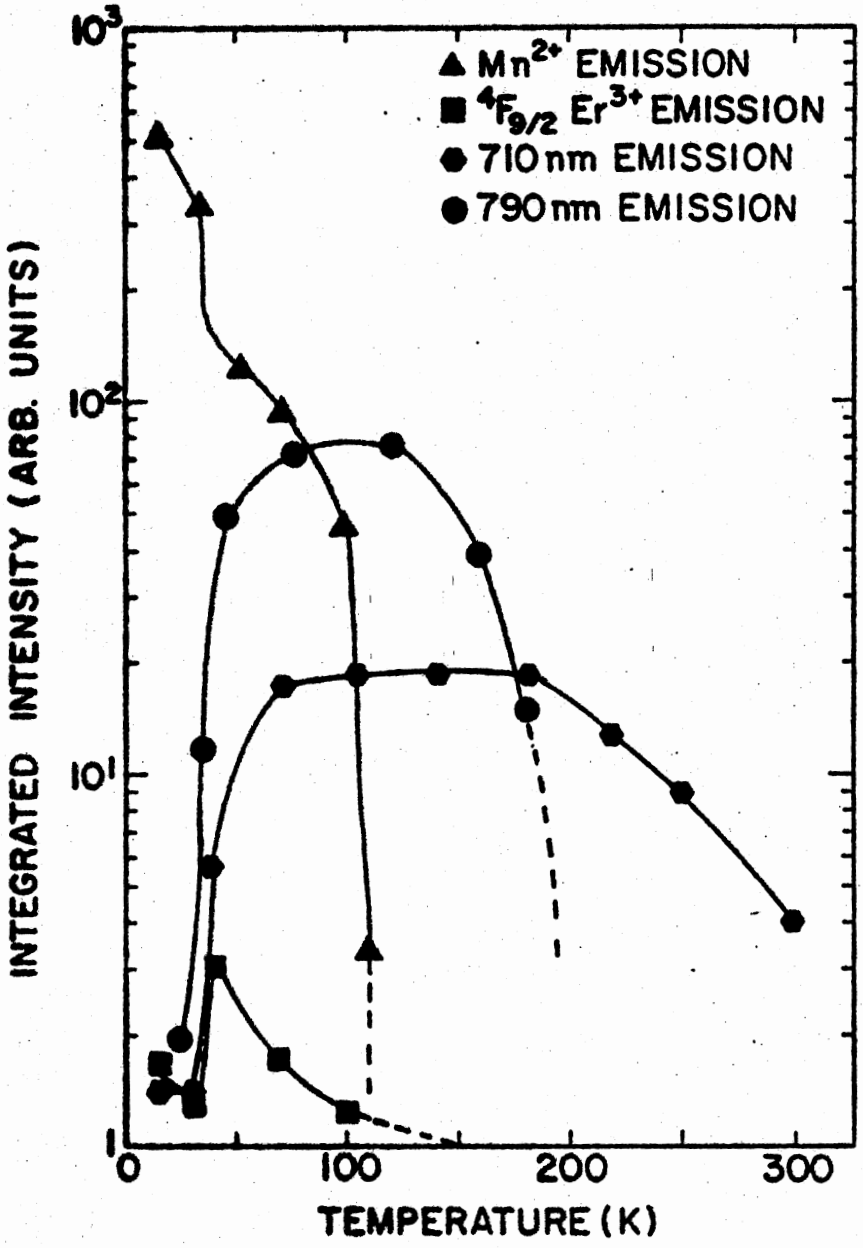

Figure 22. Integrated Intensity Versus Temperature for the Four Observed Bands in Figure 21

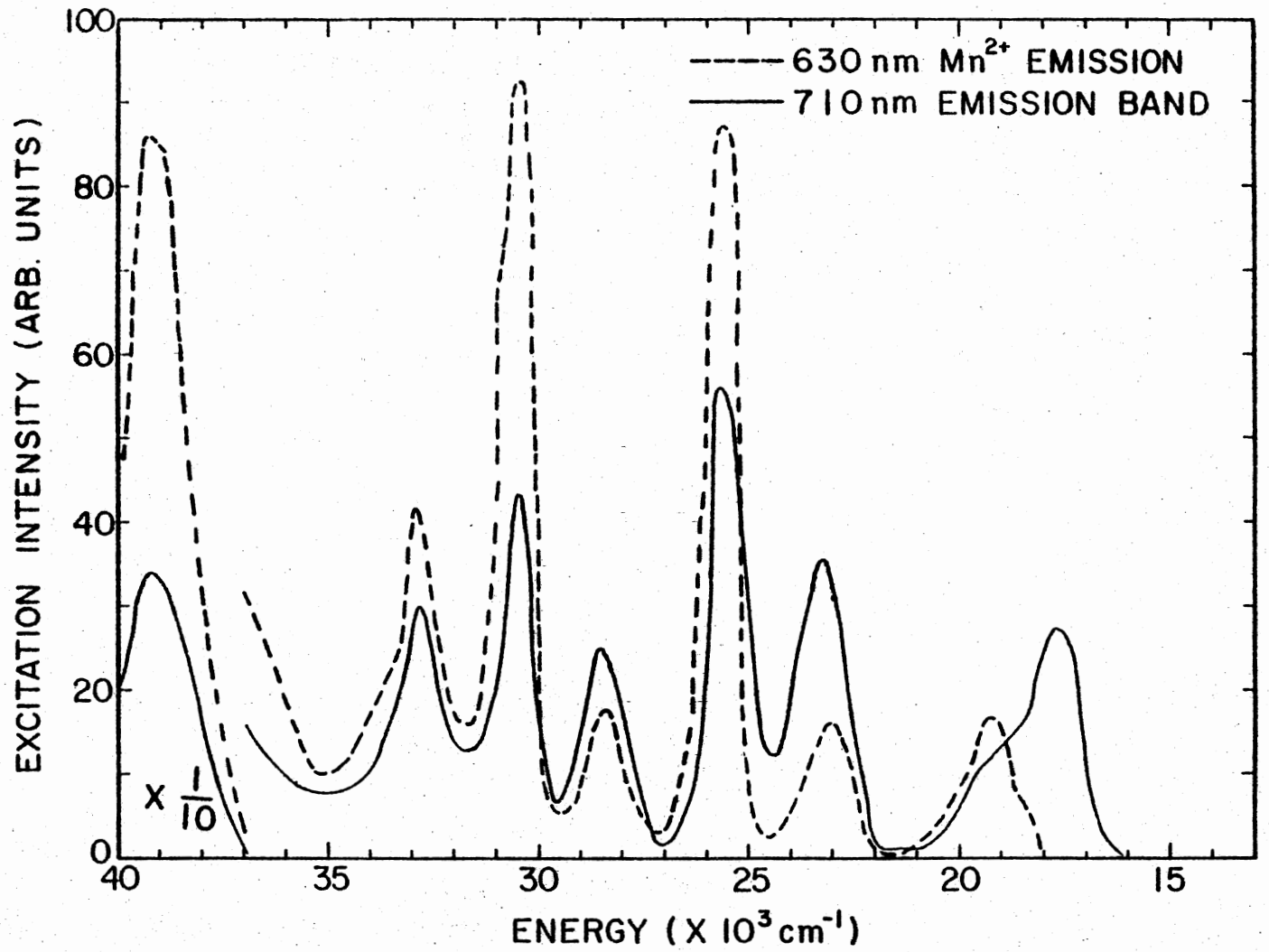

Figure 23. An Excitation Spectrum for the 582 nm Mn^{2+} Emission and the 710 nm Radiation Induced Band in Figure 21

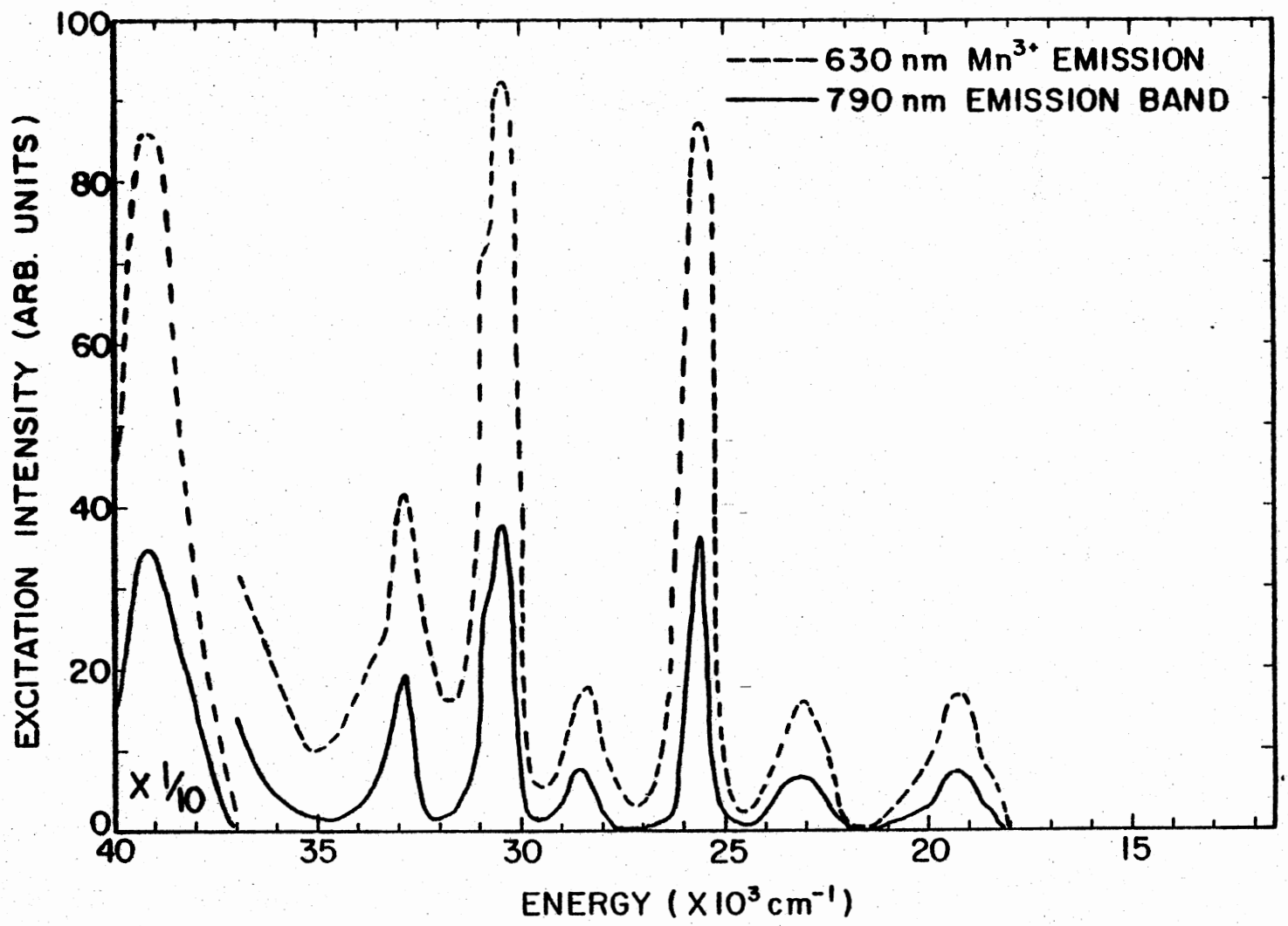

Figure 24. An Excitation Spectrum for the 582 nm Mn^{2+} Emission and the 790 nm Radiation Induced Band in Figure 21

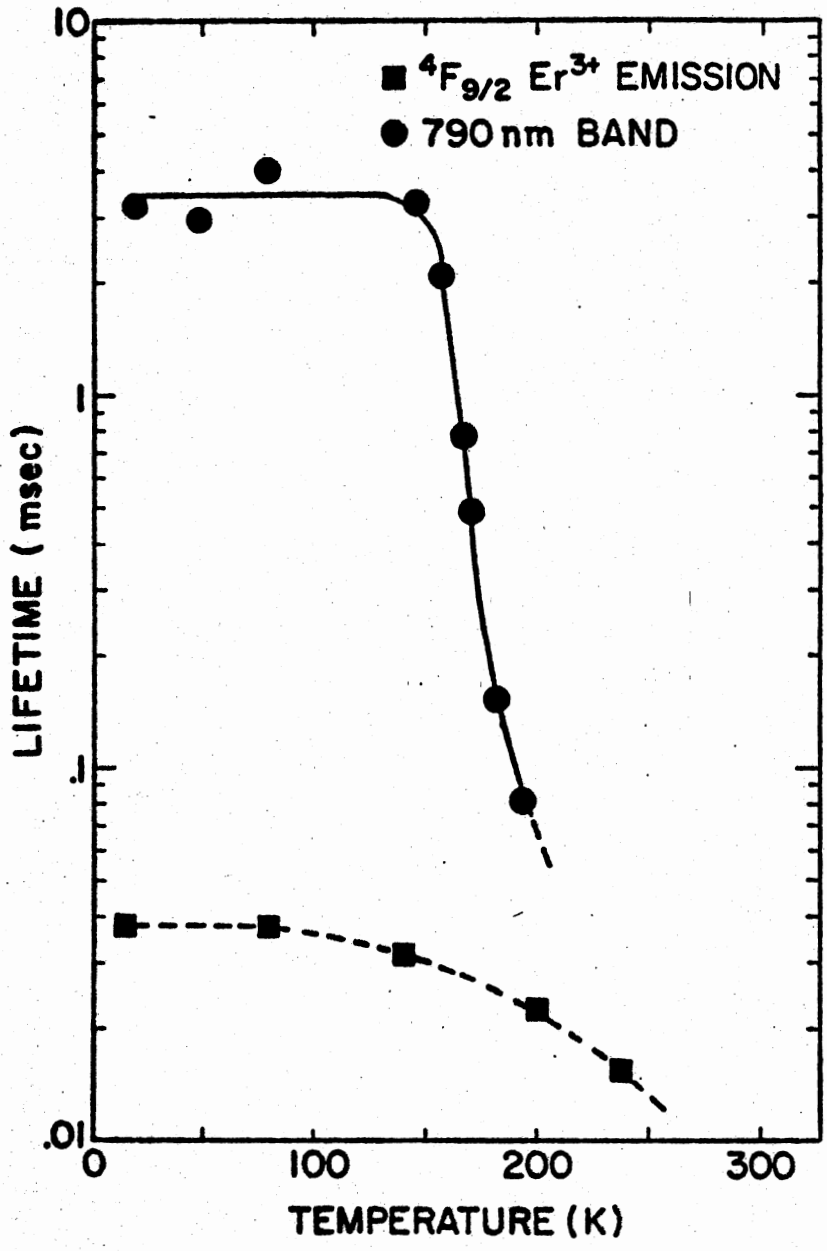

Figure 25. A Temperature Dependence of the Lifetime for the Er^{3+} Emission and the 790 Radiation Induced Band Shown in Figure 21

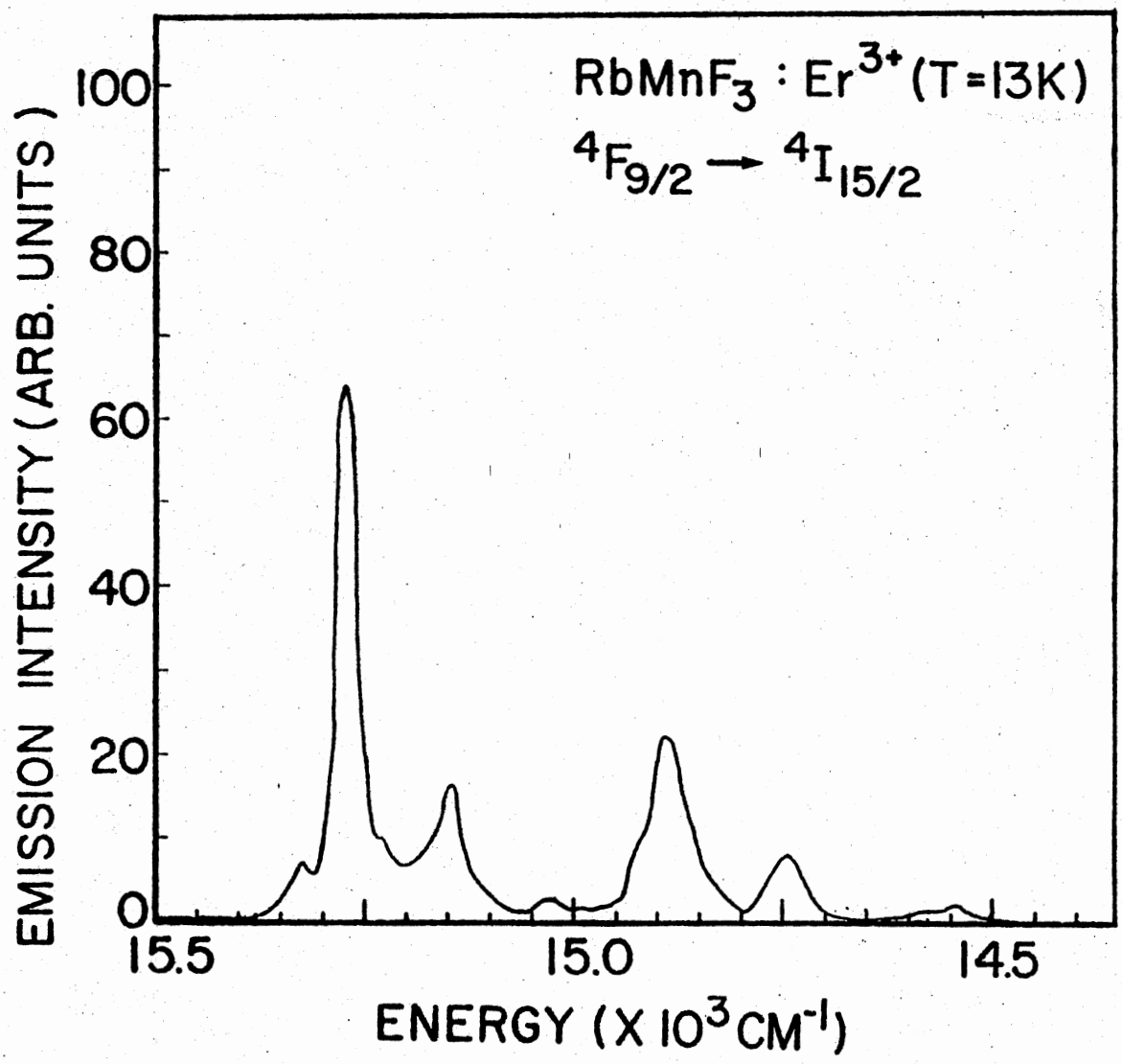

Figure 26. $^4F_{9/2}$ Er^{3+} Emission Spectrum After Irradiation with 1.7 M.e.V. Electrons for 30 Minutes

in Figure 16. In addition the temperature dependence of the integrated intensity in Figure 22 and the lifetime in Figure 25 are similar to that in the unirradiated case.

CHAPTER V

DISCUSSION

Manganese Emission

In earlier work (39), crystals like $RbMnF_3$ contained a few ppm of impurities such as Ca, Zn, and Mg. Distinct zero phonon lines are associated with each type of impurity for the perturbed Mn^{2+} emission at 582 nm (39,43). It is not known at this time what type of defect or impurity is responsible for the perturbed Mn^{2+} emission at 630 nm. Since the excitation spectra of these bands are the same and are identical with the Mn^{2+} intrinsic absorption, it is clear that energy transfer occurs from unperturbed ions, which have very long lifetimes when compared to the perturbed ions. As the sample temperature is increased, energy transfer is enhanced. The fitting of the temperature dependence of the lifetime of 582 nm emission by an "activation type" curve (Equation 15) with Δ as an activation energy is possible, but the existence of different values of Δ for the various crystals suggests that the levels are perturbed by impurities and/or mechanical strain.

Erbium Emission

When an Er^{3+} ion substitutes for an Mn^{2+} ion in $RbMnF_3$, it has O_h symmetry unless the charge compensating defect (vacancy) is close by. If O_h symmetry is assumed, then the crystal field should split the $^4F_{9/2}$

level into three levels with the $^4I_{11/2}$ level into four and the $^4I_{13/2}$ and $^4I_{15/2}$ into five levels each (13). This indicates that the ground state should have at least five levels upon which emission from an excited state can terminate. In Figure 16, the emission from the $^4F_{9/2}$ and $^4I_{11/2}$ excited states have been aligned to determine if five bands can be detected in both, which agree, and may be due to transitions to the five ground state levels. From other work it is expected that the total extent of the spectrum will be about 750 cm^{-1} (46). This is also the extent of the spectra shown in Figure 6. It is also evident, however, that because the excited state levels are in close proximity, thermal population of these levels is possible. This complicates the picture considerably. For example, the temperature dependence of the major peaks in Figure 6 differ. Although there is a suggestion that bands with energy separations of 150 cm^{-1}, 300 cm^{-1}, 550 cm^{-1}, and 700 cm^{-1} are related to the same transitions, it is not possible to be certain.

$Mn^{2+} \rightarrow Er^{3+}$ Energy Transfer

The best evidence for $Mn^{2+} \rightarrow Er^{3+}$ energy transfer is shown in Figure 18 by the presence of manganese bands in the Er^{3+} excitation spectra. Direct excitation of the Er^{3+} absorption bands was noted, but most of the emission was a result of $Mn^{2+} \rightarrow Er^{3+}$ energy transfer. The fact that the Mn^{2+} excitation bands can be seen in the Er^{3+} excitation spectrum at room temperature suggested that the energy transfer process was nonradiative. Additional evidence for this nonradiative energy transfer was found by comparing the decrease in manganese emission

intensity between ten and fifty Kelvin with a corresponding increase in the Er^{3+} intensity in the same temperature region. This is contrary to the expected behavior for radiative energy transfer. Moreover, this increase of the Er^{3+} emission with temperature corresponds to the same temperature region in which repopulation of the intrinsic Mn^{2+} band from the 582 nm level occurs.

The model of Flaherty and Di Bartolo (45) with some modifications can be used to help explain these observations. It is possible that at very low temperatures the Mn^{2+} "exciton" is free to move through the lattice. As the temperature is raised to 20K, exciton-phonon interactions decrease the number of excitons available to interact with the Er^{3+}. This is evidenced by an initial decrease in the intensity of the Er^{3+} emission and a slight decrease in the impurity-perturbed manganese emission. At 40K the 582 nm band is thermally repopulating the number of available excitons so that the Er^{3+} emission increases. As the temperature is raised further, exciton-phonon interactions and Er^{3+}-phonon interactions become increasingly competitive. The result is a decrease in the Er^{3+} emission. Clearly this suggested model warrants further experimental investigation.

Construction of a Configurational Coordinate Diagram

The absorption, emission, and lifetime data presented in Chapter IV are complete enough to attempt to construct a set of configuration coordinate curves for the lower levels of Er^{3+} in $RbMnF_3$ with the help

of the theory of Struck and Fonger (53-57) which was discussed in Chapter II. Nonradiative rates calculated from this theory will be compared with the model of Flaherty and Di Bartolo (46) which requires only the lifetimes and integrated intensities at two different temperatures for two levels.

The predicted lifetimes may be found by using Equation 14 in Chapter II. An estimate of N_{uv} can be obtained from the compliance constants measured for $RbMnF_3$ at 4.2K (86). A maximum value for N_{uv} was found to be 1.31×10^{13} sec^{-1}. For these calculations a N_{uv} of 1×10^{13} sec^{-1} was used for all cases. An analysis of the temperature dependence of the $^4I_{13/2}$ lifetime can now be made.

Since Er^{3+} is shielded by the 5s and 5p orbitals, a first approach to constructing a configuration coordinate diagram is to assume $\theta = 45^o$, i.e. all the levels have the same interacting phonon frequency. An interacting phonon frequency of 267 cm^{-1} was used. This number is in good agreement with the infrared reflectivity data of Perry and Young (87). From the absorption and emission peaks, a_{uv} was found to be 0.38. From the zero phonon energy p_U is approximately 24, thus taking p_U=24; $a_{uv} = 0.38$, $\hbar\omega_v = 267$ cm^{-1}, $\theta = 45^o$, and $N_{uv} = 1 \times 10^{13}$ sec^{-1} a temperature independent lifetime was found as evidenced by the straight line in Figure 19. These data can also be used along with an effective mass of six fluorines to construct a configuration coordinate diagram as shown in Figure 27. In the figure, it can be seen that the $^4I_{13/2}$ parabola does not cross the ground state parabola.

Next we consider the $^4I_{11/2}$ level which has nonradiative decay only to the $^4I_{13/2}$ level. Clearly p_U will be smaller in this case due

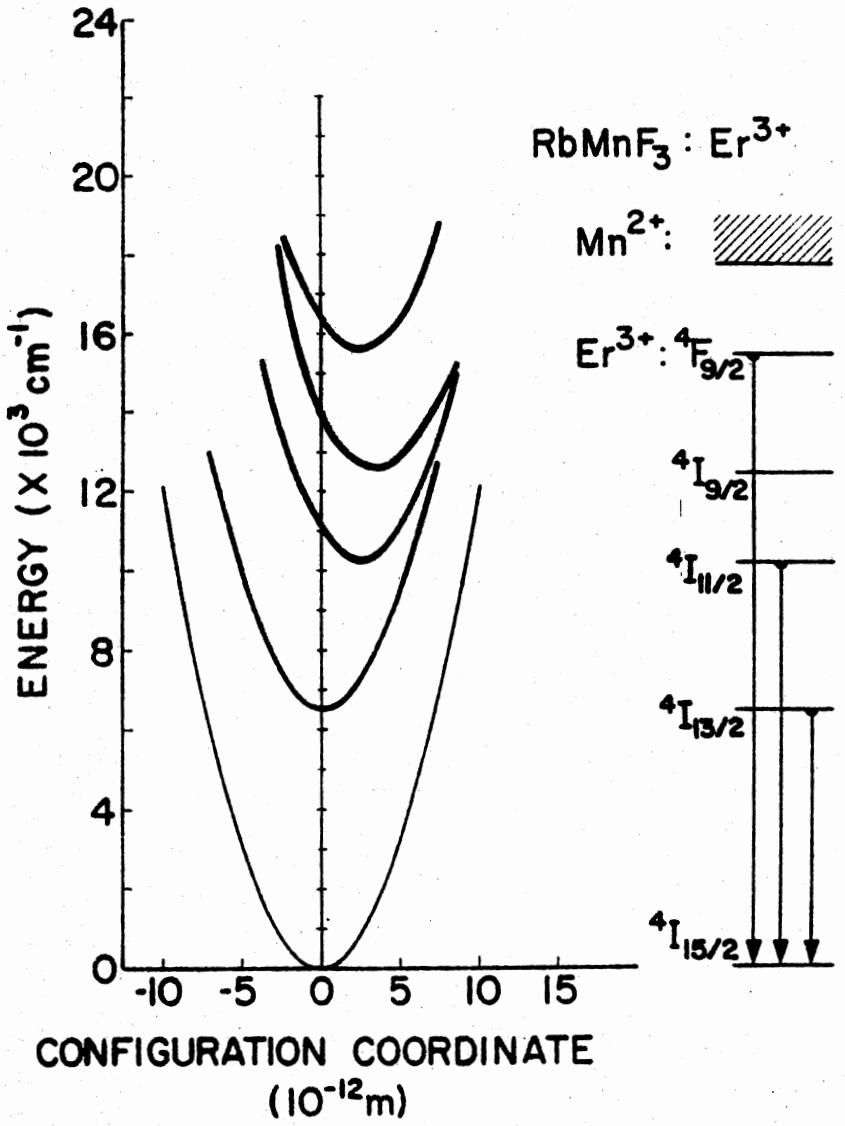

Figure 27. A Configurational Coordinate Diagram for the Lower Levels of Er^{3+} in $RbMnF_3$

to the smaller energy gap. The best obtained fit is illustrated by the broken line in Figure 9. Actual experimental and theoretical values together with other paraboli such as U_{p_U}, $\langle m \rangle_{p_U}$, $\langle m \rangle_v$, E_{p_U} (cm^{-1}), and A_{p_U} are given in Table III. a_{uv} in this "best" fit case is the relative displacement of the $^4I_{11/2}$ parabola with respect to the $^4I_{13/2}$ parabola. Again from absorption and emission peak positions an absolute displacement between the $^4I_{11/2}$ parabola and the ground state parabola of 2.3 can be determined. This is approximately the sum of 0.38 and 1.9.

For the case of the temperature quenching of the lifetime for the $^4F_{9/2}$ emission, it is assumed that the $^4F_{9/2}$ nonradiatively feeds only the $^4I_{9/2}$. The best fit for the QMSCC model to the data is illustrated by the dashed line in Figure 19. A summary of the various parameters is given in Table IV. An a_{uv} of 1.49 represents the relative displacement of the $^4F_{9/2}$ parabola from the $^4I_{9/2}$ parabola. From absorption and emission measurements, the absolute displacement of the $^4F_{9/2}$ parabola is 1.93. Looking at the ^4I_J parabola constructed so far, it seems physically reasonable that for increasing J the paraboli should be increasingly offset from zero. With this in mind, the absolute displacement of the $^4I_{9/2}$ can be estimated as 1.93 + 1.49 = 3.42. The displacement of the $^4I_{11/2}$ was found previously to be 2.28. Thus the following parameters should be inserted into Struck and Fonger's U.V. matrix method to predict the nonradiative rate between the $^4I_{9/2}$ and the $^4I_{11/2}$ ($\theta = 45^o$, $a_{uv} = 3.42 - 2.28 = 1.14$, $p_U = 8$, $h\omega_v = 267$ cm^{-1} and $N_{uv} = 1 \times 10^3$ sec^{-1}). The results predicted from these parameters are given in Table V.

TABLE III

RESULTS OBTAINED USING STRUCK AND FONGER'S U.V. MATRIX METHOD FOR THE $^4I_{11/2} \rightarrow {}^4I_{15/2}$ EMISSION OF Er^{3+} IN $RbMnF_3$. THE PARAMETERS USED ARE AS FOLLOWS: $p_U = 14$, $a_{uv} = 1.9$, $\hbar\omega_v = 267\ cm^{-1}$, $\theta = 45^o$ AND $N_{uv} = 1 \times 10^{13}\ SEC^{-1}$

T(K)	U_{p_U} (X 10^{-12})	$\langle m \rangle_{p_U}$	$\langle m \rangle_v$	E_{p_U} (cm^{-1})	A_{p_U} (sec^{-1})	$\tau_{exp.}$ (msec)	$\tau\tau_{calc.}$ (msec)
15	1.11	9.4×10^{-12}	7.1×10^{-12}	2.31×10^{-8}	19.1	8.4	9
40	1.11	8.8×10^{-4}	6.6×10^{-5}	.214	19.23	10	9
52	1.12	8.1×10^{-3}	6.1×10^{-4}	1.97	20.3	7.9	9
70	1.16	.054	4.1×10^{-3}	13.3	26.4	8.3	9
87	1.28	.16	.012	39.2	42.4	9.7	8.9
125	1.97	.63	.048	155.5	2.03	7.5	8.4
175	4.61	1.63	.125	397	2×10^3	7.3	6.8
200	7.48	2.22	.17	541	6.3×10^3	6.0	5.7
210	9.11	2.46	.19	602	9.1×10^3	6.1	5.2
236	15.29	3.13	.243	763.8	2.7×10^4	5.15	4
247	19.03	3.42	.266	834	4.2×10^4	5.4	3.4
260	24.62	3.76	.294	917	6.8×10^4	3.7	2.9
278	35.06	4.24	.334	1035.4	1.3×10^5	1	2.2
297	52.57	4.81	.381	1173.4	2.5×10^5	.75	1.6

TABLE IV

RESULTS OBTAINED USING STRUCK AND FONGER'S U.V. MATRIX METHOD FOR THE $^4F_{9/2} \rightarrow {}^4I_{15/2}$ EMISSION OF Er^{3+} IN $RbMnF_3$. THE PARAMETERS USED ARE AS FOLLOWS: $p_U = 10$, $a_{uv} = 1.49$, $\hbar\omega_v = 267\ cm^{-1}$, $\theta = 45^o$ and $N_{uv} = 1 \times 10^{13}\ SEC^{-1}$

T(K)	U_{p_U} (X 10^{-9})	$\langle m \rangle_{p_U}$	$\langle m \rangle_v$	E_{p_U} (cm^{-1})	A_{p_U} (X 10^3 sec^{-1})	$\tau_{exp.}$ (μsec)	$\tau_{calc.}$ (μsec)
13	.44	1.36×10^{-12}	1.37×10^{-13}	3.27×10^{-10}	4.38	39.6	34.4
50	.44	4.5×10^{-3}	4.53×10^{-4}	1.07	4.54	40.5	34.4
72	.46	.047	4.8×10^{-3}	11.4	5.75	40.5	34.4
100	.53	.215	.022	51.6	11.1	40.0	33.3
116	.61	.37	.037	88.96	18.4	39.7	32.4
140	.79	.67	.068	161.3	41.5	35.0	30.7
187	1.46	1.43	.146	341	205	24.5	25.4
197	1.69	1.61	.165	385	284	25	24.0
215	2.19	1.95	.2	466	500	20	21.4
240	3.16	2.43	.25		1,044	15.0	17.7

TABLE V

PREDICTED RESULTS FROM STRUCK AND FONGER'S U.V. MATRIX METHOD FOR THE $^4I_{9/2}$ AND $^4I_{11/2}$ LEVELS OF Er^{3+} IN $RbMnF_3$. THE PARAMETERS USED ARE AS FOLLOWS: $p_U = 8$, $a_{uv} = 1.14$, $\hbar\omega = 267\ cm^{-1}$, $\theta = 45^\circ$ AND $N_{uv} = 1 \times 10^{13}\ SEC^{-1}$

T(K)	U_{p_U} (X 10^{-9})	$\langle m \rangle_{p_U}$	$\langle m \rangle_v$	E_{p_U} (cm^{-1})	A_{p_U} (X 10^4 sec^{-1})	$N_{uv} \cdot U_{p_U}$ (X 10^4 sec^{-1})
15	2.23	5.96×10^{-11}	7.13×10^{-12}	1.39×10^{-8}	2.22	2.23
40	2.23	5.52×10^{-4}	6.6×10^{-5}	.12	2.23	2.23
52	2.24	5.1×10^{-3}	6.1×10^{-4}	1.2	2.31	2.24
70	2.29	.03	4.1×10^{-3}	8	2.7	2.29
87	2.43	.1	.01	23.7	3.6	2.43
125	3.14	.4	.05	94	9.3	3.14
175	5.26	1	.12	242	38.7	5.26
200	7.05	1.4	.17	330	76.6	7.05
210	7.95	1.6	.19	368	99.5	7.95
236	10.88	2.0	.24	468	190	10.88
247	12.44	2.2	.26	512	247	12.44
260	14.55	2.4	.29	564	333	14.55
278	18.05	2.7	.33	638	500	18.05
299	23.14	3.1	.38	725	770	23.14

The nonradiative rate for the levels at low temperatures can now be plotted versus the energy gap between these different levels. This is shown in Figure 28. Note that the predicted nonradiative rate between the $^4I_{9/2}$ and $^4I_{11/2}$ lies very close to the line drawn through the rates for the $^4F_{9/2}$ and $^4I_{11/2}$. Thus, Struck and Fonger's U.V. matrix method predicts an experimentally reasonable energy gap law dependence. Energy gap parameters and phonon coupling parameters are summarized in several materials containing Er^{3+} in Table VI.

Now that a configuration coordinate diagram (Figure 27) has been constructed, it should be pointed out that the lack of emission from the $^4I_{9/2}$ level can be explained by the relatively low intersection of the $^4I_{9/2}$ with the $^4I_{11/2}$. This is consistent with the high nonradiative rates in Table V.

As mentioned earlier, Flaherty and Di Bartolo (46) have developed an expression to determine the nonradiative transition rate between two levels A and B. It seems prudent to compare their method with the QMSCC model. The time dependence of the rise in $^4I_{13/2}$ intensity is controlled by the nonradiative rate p_{AB} between the $^4I_{11/2}$ (A) and $^4I_{13/2}$ (B) paraboli and the lifetime of the $^4I_{11/2}$. Using the following two rate equations

$$\frac{dn_A}{dt} = -n_A(p_A + p_{AB}) \approx -n_A p_A \qquad (16)$$

$$\frac{dn_B}{dt} = n_A p_{AB} - n_B p_B \qquad (17)$$

Flaherty and Di Bartolo (46) developed the following expression for the time dependence of the $^4I_{13/2}$ emission

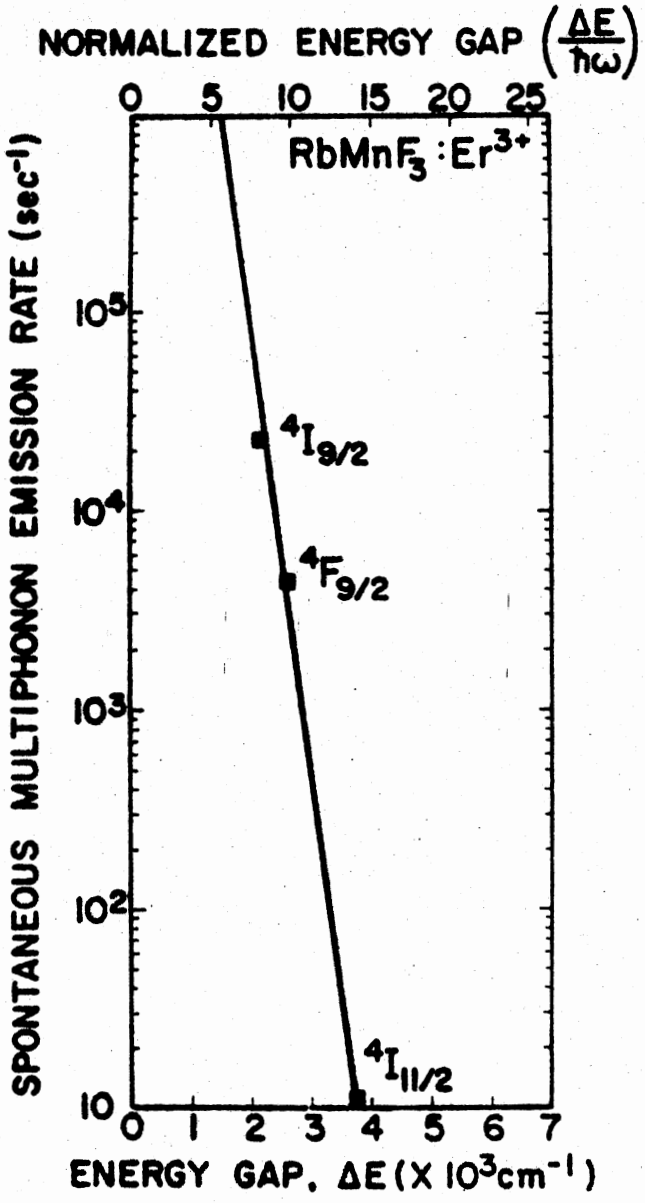

Figure 28. Spontaneous Multiphonon Transition Rate Versus Gap Energy of Er^{3+} in $RbMnF_3$

TABLE VI

ENERGY GAP LAW PARAMETERS FOR SEVERAL MATERIALS CONTAINING ERBIUM

Material	$C(sec^{-1})$	$\alpha(cm)$	ε
$RbMnF_3:Er^{3+}$	1.06×10^{9}	4.7×10^{-3}	.179
$MnF_2:Er^{3+}$ (47)	5.5×10^{7}	4.3×10^{-3}	.259
$Y_2O_3:Er^{3+}$ (64)	2.7×10^{8}	3.8×10^{-3}	.12

$$\frac{n_B(t)}{n_B(o)} = \left[1 + \frac{n_A(o)}{n_B(o)} \frac{p_{AB}}{p_A - p_B}\right] e^{-p_B t} - \frac{n_A(o)}{n_B(o)} \left[\frac{p_{AB}}{p_A - p_B}\right] e^{-p_A t} \qquad (18)$$

where

$$p_A = \frac{1}{\tau_A} \text{ and } p_B = \frac{1}{\tau_B}$$

Equation 18 can be derived by taking the Laplace transform of Equations 16 and 17 and expanding in partial fractions. At low temperatures p_{AB} can be estimated from the Struck and Fonger calculation to be 11.1 sec^{-1}, at 33K p_A = 111 sec^{-1} and p_B = 35.7 sec^{-1}. Substituting these values into Equation 18, it is seen in Figure 20 that the theory matches the experimental data. By setting the derivative of Equation 18 to zero, the time (t_{max}) the intensity takes to reach a maximum can be calculated by the following formula (46):

$$t_{max} = \frac{1}{p_A - p_A} \ln\left[\frac{p_B}{p_A} + \frac{p_B(p_A - p_B)}{p_A p_{AB}} \left(\frac{n_B(o)}{n_A(o)}\right)\right] \qquad (19)$$

Substituting the values given above and determining $n_B(o)/n_A(o)$ by normalization of Equation 18 to experiment, a value of 13.2 msec can be found. As the temperature increases, t_{max} decreases consistent with the increase in the nonradiative rate p_{AB}.

Flaherty and Di Bartolo (46) also have developed an expression for the nonradiative rate between two levels A and B using only lifetimes and integrated intensities of these levels at two different temperatures. Let level A be the $^4F_{9/2}$ level and level B be the $^4I_{11/2}$. Experimentally, emission is observed from levels A and B but not from the intermediate $^4I_{9/2}$ level. This means that the nonradiative should be much more than the radiative rate from the $^4I_{9/2}$ level. In other

words, all ions excited into the $^4I_{9/2}$ state should decay into the $^4I_{11/2}$ state. Thus, the nonradiative rate between level A and B predicted by Flaherty and Di Bartolo should reflect the rate between the $^4F_{9/2}$ and $^4F_{9/2}$ and $^4I_{9/2}$ levels. The expression developed by Flaherty and Di Bartolo is as follows:

$$P_{AB}(T_2) = \left[\frac{1}{\tau_A(T_2)} - \frac{1}{\tau_B(T_1)}\right]\left\{1 - \frac{\tau_B(T_2)}{\tau_B(T_1)}\left[\frac{I_A(T_2)}{I_B(T_2)}\right]\left[\frac{I_B(T_1)}{I_A(T_1)}\right]\right\} \quad (20)$$

For T_1 = 184K, $\tau_A(T_1)$ = .027 msec, $\tau_B(T_1)$ = 6.5 msec, $\frac{I_B(T_1)}{I_A(T_1)}$ = 2.05. In the case of T_2 = 222K, $\tau_A(T_2)$ = .02 msec, $\tau_B(T_2)$ = 5.4 msec and $\frac{I_A(T_2)}{I_A(T_2)}$ = .25. From these values a P_{AB} of 2.26 x 10^4 sec^{-1} was found. From Table IV, P_{SF} at 222K is 2.5 x 10^4 sec^{-1} which is in reasonable agreement. The nonradiative rates P_{AB} and P_{SF} may be compared absolutely at two temperatures (46) by the following expression.

$$\frac{P_{AB}(T_2)}{P_{AB}(T_1)} = \frac{\tau_B(T_1)}{\tau_B(T_2)} \quad \frac{I_A(T_1)}{I_B(T_1)} \quad \frac{I_B(T_2)}{I_B(T_2)} \quad (21)$$

$$\frac{P_{SF}(T_2)}{P_{SF}(T_1)} = \frac{N_{uv} U_{P_U}(T_2)}{N_{uv} U_{P_U}(T_1)} = \frac{U_{P_U}(T_2)}{U_{P_U}(T_1)} \quad (22)$$

again from Table IV at 215K P_{SF} (184) = 1.45 x 10^4 sec^{-1}. Substituting the numbers into Equations 21 and 22

$$\frac{U_{P_U}(T_2)}{U_{P_U}(T_1)} = 1.72 \text{ while } \frac{P_{AB}(T_2)}{P_{AB}(T_1)} = 2.34$$

Thus the configuration coordinate model predicted by the use of Struck and Fonger is within 25% of the Flaherty and Di Bartolo calculation.

It would be possible to match the two calculations exactly by choosing a lower N_{uv} value for the Struck and Fonger model.

Trapping Model and Irradiated Results

For unirradiated $RbMnF_3:Er^{3+}$, Er^{3+} ions and impurity perturbed Mn^{2+} ions act as traps for the exciton band. This is shown schematically in Figure 5. The interaction between the exciton band and the Er^{3+} ions was discussed in the section on $Mn^{2+} \rightarrow Er^{3+}$ energy transfer. Two defect perturbed Mn^{2+} bands were observed at 582 nm and 630 nm. The sharp drop in intensity and lifetime in Figures 13 and 14 can be explained by thermal repopulation of the exciton band. A similar explanation can be given for the quenching of the 630 nm band near 110K. In this case, however, there are several different types of sites contributing to the emission since the temperature quenching of the lifetime cannot be fit with a single activation formula like Equation 15.

Irradiation with 1.7 M.e.V. electrons for 30 minutes at 300K introduces two new traps for the exciton band at 710 nm and 790 nm. In Figure 22 the increases in the intensity of the 710 nm and 790 nm bands correspond with the thermal repopulation of the exciton band by the impurity perturbed Mn^{2+} ions. The stability of the 710 nm band to fairly high temperatures versus the 790 nm band can be explained by different trapping cross sections for these two bands. The final decrease in intensity for this 710 nm band is due to feeding of quenching traps in the near infrared.

The temperature dependence of the Er^{3+} emission, lifetimes, excitation spectra and emission spectra are very similar to the unirradiated

case. In addition no evidence was seen for Er^{2+}. This suggests that the shielding 5s and 5p orbitals are very effective for the irradiated $RbMnF_3:Er^{3+}$. In CaF_2 doped with Er^{3+} 10% of the Er^{3+} changed to Er^{2+} after irradiation (88).

Upconversion

Upconversion is a process where two infrared photons are converted into a visible photon. This concept was first conceived by Bioembergen (89) as an Infrared Quantum Counter (IRQC). The small, sharp rare earth absorption bands in this device limited practical efficiencies. The next major step came in 1966 when Auzel (90) and independently Ovsyankin and Feofilov (91) sensitized the upconversion process by the introduction of ytterbium ions. An example of this is shown in Figure 29 after the work of Auzel (92). Basically excitation of the three upper Er^{3+} levels is obtained first through absorption by a Yb^{3+} ion at .97 micron. Excitation of the $^4I_{11/2}$ level of Er^{3+} is obtained from the $^4F_{5/2}$ level of Yb^{3+} through resonant energy transfer. A second .97 micron photon is then absorbed either by the same Yb^{3+} ion or another nearby Yb^{3+} ion in the $^4F_{7/2}$ state which transfers its energy to the Er^{3+}. Emission is finally observed from the levels indicated. Excellent reviews of Yb^{3+}-rare earth couples are available in the literature (92,93,63).

In contrast to the typical Yb^{3+}-rare earth couples another possibility is shown in Figure 30. From the work of Wilson et al. (48), it is known that the $^4S_{3/2}$ level of Er^{3+} transfers its energy to the Mn^{2+} exciton band. This energy may then be dissipated by radiation induced impurity perturbed Mn^{2+} ions with a short lifetime. Thus the populatation of the $^4S_{3/2}$ level is important. Two possibilities for excitation

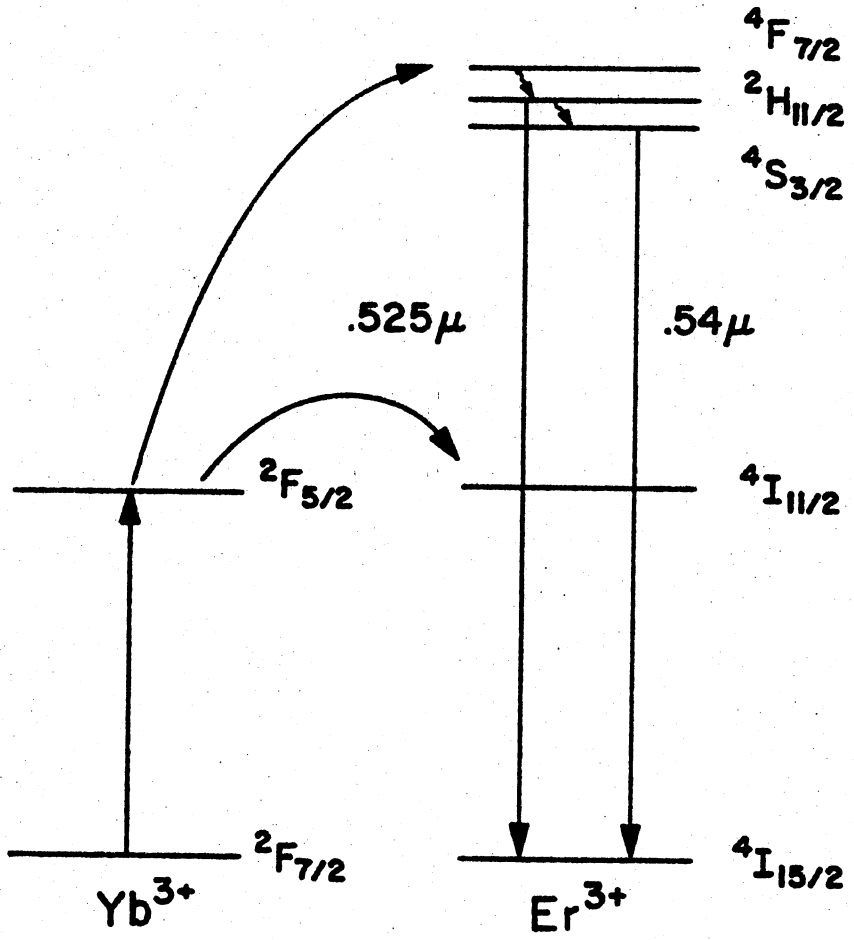

Figure 29. An Example of a Conventional Yb^{3+}-Rare Earth Upconversion Process

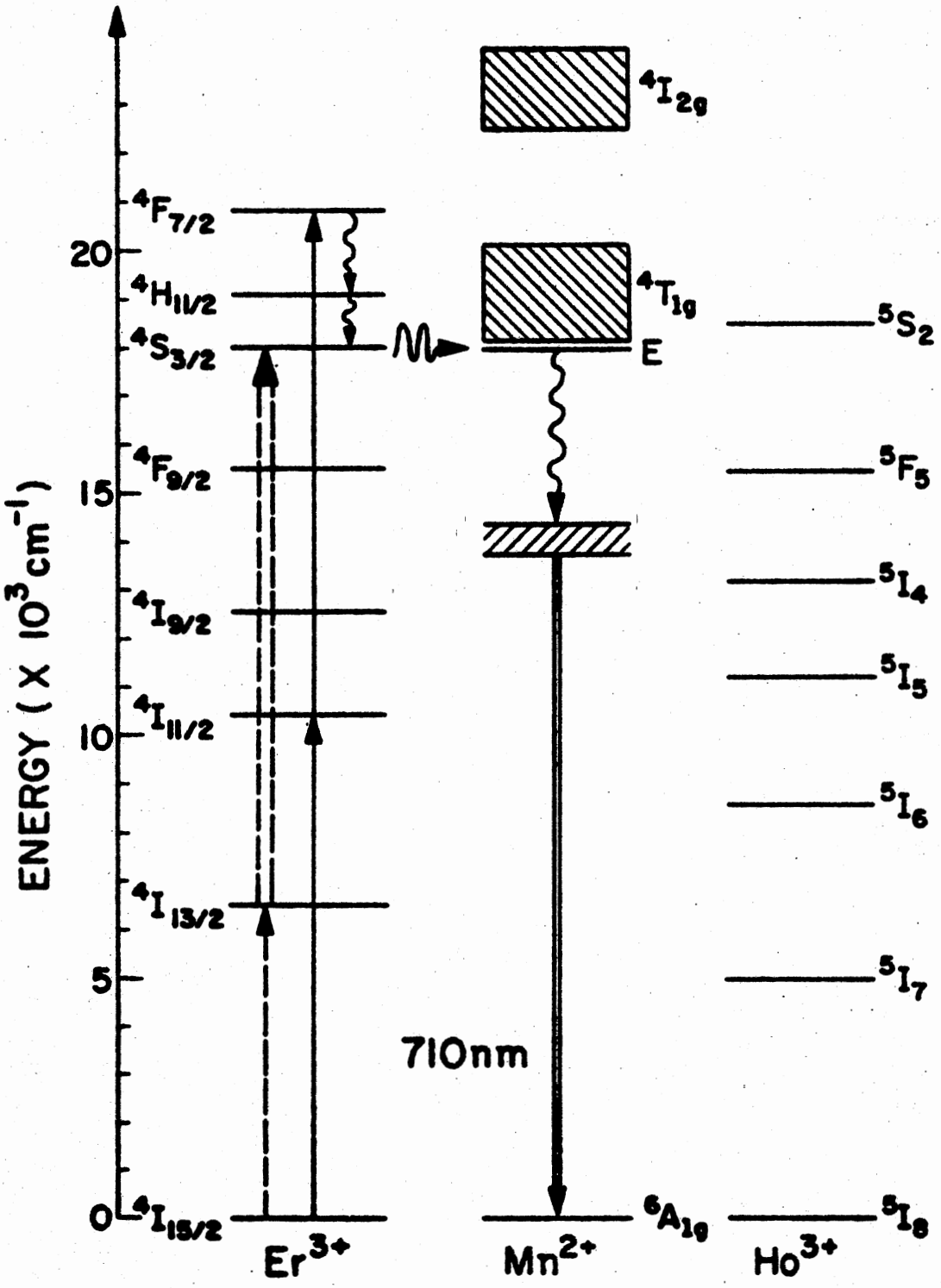

Figure 30. The Proposed Rare Earth-Radiation Perturbed Mn^{2+} Upconversion and IRQC Processes

of the $^4S_{3/2}$ level are shown in Figure 30. Note that both intermediate states have a relatively long experimentally measured lifetime. In the solid line, the $^4I_{11/2}$ level is excited to the $^4F_{7/2}$ level of Er^{3+}. Er^{3+} clustering would clearly help this process. In the dotted line the $^4I_{13/2}$ level is populated with infrared light. Use of an external source such a laser then populates the upper levels of Er^{3+}. This suggested process obviously warrants further investigation in this material and similar materials like $MnF_2:Er^{3+}$ and in general.

CHAPTER VI

CONCLUSIONS AND PROBLEMS FOR FURTHER STUDY

The following conclusions may be drawn from the data and discussion of unirradiated $RbMnF_3:Er^{3+}$ in Chapters IV and V:

1. A small effect due to the presence of Er^{3+} on the Mn^{2+} emission was noted when the temperature dependence of the lifetimes was compared for $RbMnF_3$ and $RbMnF_3:Er^{3+}$.

2. No emission was observed from the $^4I_{9/2}$ or $^4S_{3/2}$ levels of Er^{3+} in $RbMnF_3$.

3. The temperature dependence of the emission integrated intensity and excitation spectra indicated nonradiative $Mn^{2+} \rightarrow Er^{3+}$ energy transfer.

4. The $^4I_{13/2}$ and $^4I_{11/2}$ emissions of Er^{3+} were found to have lifetimes between 0.75 and 35 milliseconds.

5. The U.V. matrix method of Struck and Fonger, together with absorption and emission energies were used to construct a configuration coordinate diagram. Nonradiative rates predicted by the Struck and Fonger analysis were compared with intensity versus time data of the $^4I_{13/2}$ and the predictions of the model of Flaherty and Di Bartolo. Good agreement was obtained.

In addition to these conclusions, the following areas should be pursued further for unirradiated $RbMnF_3:Er^{3+}$:

1. An attempt should be made to populate the $^4S_{3/2}$ level of Er^{3+} in $RbMnF_3$ by laser excitation.

2. The low temperature dip in the Er^{3+} integrated intensity versus temperature should be closely checked in other similar materials.

3. A range of Struck and Fonger parameters could be found by comparing different materials doped with Er^{3+} such as $KMnF_3$, $BaMnF_3$, and MnF_2.

For irradiated $RbMnF_3:Er^{3+}$ two irradiation defect bands were observed at 710 nm and 790 nm after 300K irradiation with 1.7 M.e.V. electrons. Different lifetimes, temperature dependences, and excitation spectra were observed. The 710 nm band was excited either by energy transfer from the manganese or by direct excitation. No evidence was seen for perturbation of Er^{3+} or a valence change to Er^{2+}. Further work should consider a defect production mechanism for $RbMnF_3:Er^{3+}$. In addition, low temperature irradiation measurements should be taken.

REFERENCES

(1) Markham, J. J., Solid State Physics, Suppl. 8 (Academic Press, York, 1966).

(2) Vehse, W. E., W. A. Sibley, F. J. Keller and Y. Chen, Phys. Rev. 167, 828 (1968).

(3) Hersch, H. N. and L. Bronstein, Am. J. Phys. 25, 306 (1957).

(4) Sonder, E. and W. A. Sibley, in Point Defects in Solids, ed. J. Crawford and L. M. Slifkin (Plenum, New York, 1972).

(5) Becquerel, J., Radium 4, 328 (1907).

(6) Bethe, H., Z. Physik 60, 218 (1930).

(7) Kramers, H. A., Proc. Acad. Sci. Amsterdam 32, 1176 (1930).

(8) Van Vleck, J. A., J. Phys. Chem. 41, 67 (1937).

(9) Dieke, G. H., in Advances in Quantum Electronics ed. J. R. Singer (Columbia University Press, New York, 1961).

(10) Dieke, G. H., Spectra and Energy Levels of Rare Earth Ions in Crystals (Interscience, New York, 1968).

(11) Hufner, S., Optical Spectra of Transparent Rare Earth Compounds (Academic Press, New York, 1978).

(12) Wybourne, B. G., Spectroscopic Properties of Rare Earths (Inter-Science, New York, 1965).

(13) Di Bartolo, B., Optical Interactions in Solids (John Wiley and Sons, New York, 1968).

(14) Bethe, H. A., Ann. Physik 3, 133 (1929).

(15) Van Vleck, J. H., J. Chem. Phys. 8, 787 (1940).

(16) Finkelstein, R. and J. H. Van Vleck, J. Chem. Phys. 8, 790 (1940).

(17) Hartmann, H. and H. L. Schlaefer, Z. Phys. Chemie 197, 116 (1951).

(18) Ilse, F. E. and H. Hartmann, Z. Phys. Chemie 197, 239 (1951).

(19) Hartmann, H., F. E. Ilse, and H. L. Schlaefer, Z. Naturforsch 6a, 751 (1951).

(20) Orgel, L. E., J. Chem. Phys. 23, 1004 (1955).

(21) Orgel, L. E., J. Chem. Phys. 23, 1819 (1955).

(22) Orgel, L. E., J. Chem. Phys. 23, 1824 (1955).

(23) Tanabe, Y. and S. Sugano, J. Phys. Soc. Japan 9, 753,766 (1954).

(24) Sugano, S., Y. Tanabe and H. Kamimura, Multiplets of Transition Metal Ions in Crystals (Academic, New York, 1970).

(25) Ballhausen, C. J., Introduction to Ligand Field Theory (McGraw-Hill, New York, 1962).

(26) Owen, J., Proc. Roy. Soc. of London A227, 183 (1955).

(27) Griffith, J. S., The Theory of Transition Metal Ions (Cambridge Univ. Press, Cambridge, 1961).

(28) McClure, D. S., Solid State Physics 9, 399 (1959) ed. by F. Seitz and D. Turnbull (Academic, New York).

(29) Hush, N. S. and R. J. M. Hobbs, Progress in Inorganic Chemistry 10, 259 (1968), ed. by F. A. Cotton (Interscience, New York).

(30) Ferguson, J., Progress in Inorganic Chemistry 12, 159 (1970), ed. by S. J. Lippard (Interscience, New York).

(31) Iverson, M. V. and W. A. Sibley, J. of Lum. 20, No. 3 (1979).

(32) Mehra, A. and P. Vehkateswarlu, J. Chem. Phys. 47, 2334 (1967).

(33) Ferguson, J., Aust. J. Chem. 21, 307 (1968).

(34) Jorgensen, C. K., Acta Chem. Scand. 9, 405 (1955).

(35) Holloway, W. W., M. Kestigan, R. Newman and E. W. Prohofsky, Phys. Rev. Lett. 11, 82 (1963).

(36) Holloway, W. W., E. W. Prohofsky and M. Kestigan, Phys. Rev. 139A, 954 (1965).

(37) Holloway, W. W., and M. Kestigan, Phys. Stat. Sol. 28, K159 (1969).

(38) Klasens, H. A., P. Zalm and F. O. Huysman, Phillips Res. Rept. 8, 441 (1953).

(39) Green, R. L., D. D. Sell, R. S. Feigelson, G. F. Imbusch and H. J. Guggenheim, Phys. Rev. 171, 600 (1968).

(40) Gooen, K., B. Di Bartolo, M. Alam, R. C. Powell and A. Linz, Phys. Rev. 177, 615 (1969).

(41) Koumvakalis, N., W. A. Sibley and G. F. Venikouas, J. of Lum. 15, 283 (1977).

(42) Yun, S. I., N. Koumvakalis and W. A. Sibley, J. Phys. C 10, 3987 (1977).

(43) Imbusch, G. F., in Luminescence in Inorganic Solids, edited by B. Di Bartolo (John Wiley and Sons, New York, 1978). p. 155.

(44) Matyushkin, E. V., L. L. Kukushkin and V. V. Eremenko, Phys. Status Solidi 22, 65 (1967).

(45) Flaherty, J. M. and B. Di Bartolo, Phys. Rev. B8, 5232 (1973).

(46) Flaherty, J. M. and B. Di Bartolo, J. of Lum. 8, 51 (1973).

(47) Flaherty, J. M. and B. Di Bartolo, Colloques Interactionaux du C.N.R.S. No. 255, 191 (1977).

(48) Wilson, B. A., W. M. Yen, J. Hegarty and G. F. Imbusch (to be published).

(49) Eremenko, V. V., E. V. Matyushin and S. V. Petrov, Phys. Status Solidi 18, 683 (1966).

(50) Eremenko, V. V. and E. V. Matyushkin, Opt. Spectrosc. 23, 234 (1967).

(51) Hirano, M. and S. Shionoya, J. Phys. Soc. Japan 28, 926 (1970).

(52) Shionoya, S. and M. Hirano, Phys. Letters 26A, 533 (1968).

(53) Struck, C. W. and W. H. Fonger, J. of Lum. 10, 1 (1975).

(54) Fonger, W. H. and C. W. Struck, Phys. Rev. B11, 3251 (1975).

(55) Struck, C. W. and W. H. Fonger, J. of Lum. 14, 253 (1976).

(56) Fonger, W. H. and C. W. Struck, J. of Chem. Phys. 60, 1994 (1974).

(57) Fonger, W. H. and C. W. Struck, J. of Lum. 17, 241 (1978).

(58) Watts, R. K., Point Defects in Crystals (John Wiley and Sons, New York, 1977) p. 2.

(59) Yun, S. I. Ph.D. Thesis (Oklahoma State University, 1973).

(60) Cotton, F. A., Chemical Applications of Group Theory (John Wiley and Sons, New York, 1971).

(61) Watts, R. K., in Optical Properties of Ions in Solids ed. by B. Di Bartolo (Plenum Press, New York, 1975) pp. 307,337.

(62) Reisfeld, R., Structure and Bonding 30, 65 (1976).

(63) Wright, J. C., in Topics in Applied Physics ed. by F. K. Fong (Springer-Verlag, Berlin, 1976).

(64) Riseberg, L. A. and M. J. Weber, in Progress in Optics, Vol. XIV ed. by E. Wolf (North Holland, Amsterdam, 1976) p. 89.

(65) Forster, T., Ann. Phys. 2, 55 (1948).

(66) Dexter, D. L., J. Chem. Phys. 21, 836 (1953).

(67) Orbach, R., in Conf. Properties of Ions in Crystals (John Wiley and Sons, New York, 1967) p. 455.

(68) Miyakawa, T., and D. L. Dexter, Phys. Rev. B1, 2961 (1970).

(69) Orbach, R., Optical Properties of Ions in Solids ed. by B. Di Bartolo (Plenum Press, New York, 1975).

(70) Perlin, Y. E., Sov. Phys. Uspekhi 6, 542, (1963).

(71) Freed, K. F., in Radiationless Processes in Molecules and Condensed Phases ed. by F. K. Fong (Springer-Verlag, Berlin, 1976).

(72) Blasse, G., in Luminescence of Inorganic Solids ed. by B. Di Bartolo (John Wiley and Sons, New York, 1978).

(73) Fong, F. K., Theory of Molecular Relaxation (John Wiley and Sons, New York, 1975).

(74) Riseberg, L. A. and H. W. Moos, Phys. Rev. Lett. 19, 1423 (1967).

(75) Dexter, D. L., Phys. Rev. 126, 1962 (1962).

(76) Chamberlain, J. R., D. H. Paxman and J. L. Page, Proc. Phys. Soc. 89, 143 (1966).

(77) Brown, M. R., J. S. Whiting and S. A. Shand, J. Chem. Phys. 43, 1 (1965).

(78) Weber, M. J., Optical Properties of Ions in Crystals eds. H. M. Crosswhite and H. W. Moos (Interscience, New York, 1966).

(79) Partlow, W. D. and H. W. Moos, Phys. Rev. 157, 252, (1967).

(80) Merkle, L. D., Ph.D. Thesis (Oklahoma State University, 1978).

(81) Stockbarger, D. C., Rev. Sci. Instr. 7, 133 (1936).

(82) Stockbarger, D. C., Discussion Faraday Soc. 5, 294 (1949).

(83) Bridgman, P. W., Proc. Am. Acad. 60, 303 (1925).

(84) Goldberg, V., V. Moncorgé, D. Pacheco and B. Di Bartolo in Luminescence in Inorganic Solids ed. by B. Di Bartolo (John Wiley and Sons, New York, 1978) p. 603.

(85) Goldberg, V., D. Pacheco, R. Moncorgé and B. Di Bartolo, J. of Lum. 18, 143 (1979).

(86) Melcher, R. L., and D. J. Bolef, Phys. Rev. 178, 864 (1969).

(87) Perry, C. M. and E. F. Young, J. Appl. Phys. 38, 4616 (1967).

(88) Hayes, W. and J. W. Twidell, Proc. Phys. Soc. (London) 82, 330 (1963).

(89) Bloembergen, N., Phys. Rev. Lett. 2, 84 (1959).

(90) Auzel, F., Compt. Rend. B, 262, 1016 (1966).

(91) Ovsyankin, V. V., and P. P. Feofilov, Soviet Phys. JETP Lett. 4, 317 (1966).

(92) Auzel, F. E., Proc. of IEEE 61, 758 (1973).

(93) Garlick, G. F., Contemp. Phys. 17, 127 (1976).

APPENDIX

FLOWCHART FOR STRUCK AND FONGER ANALYSIS

This program predicts the temperature dependence of the lifetime from seven experimentally related parameters. The predicted results from this phenomenological theory are then compared with actual experimental values. The program for this language independent flowchart is written in Basic and runs on a PDP-11 minicomputer. In addition to predicting the temperature dependence of the lifetime, a simple modification in this program could predict the temperature dependence of absorption or emission band shapes. The modification is to calculate U_{p_U} for various p_U.

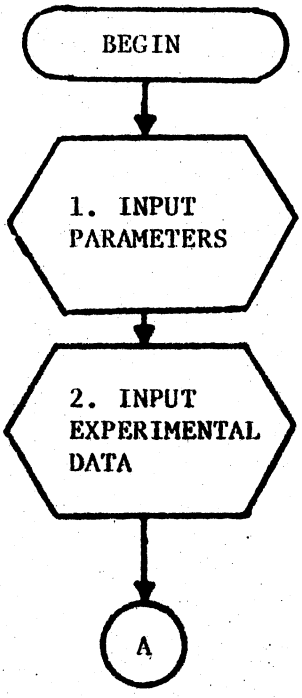

1. As explained in the text these are θ, a_{uv}, p_U, $\hbar\omega_v$, N_{uv}, and R_{uv}.

2. This includes observed lifetimes and temperatures along with the number of data points.

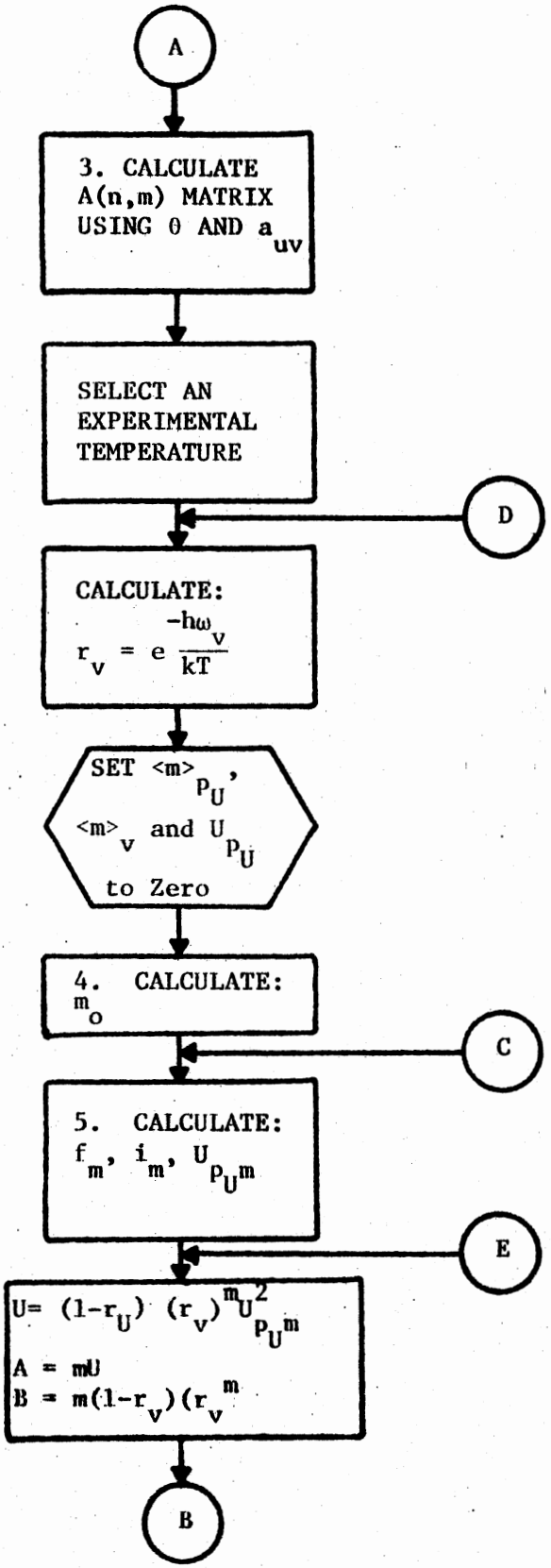

3. The A(n,m) matrix elements or overlap integrals are calculated from the Mannebach Recursion Formulas (Equations 8 and 9)

4. This section is described later

5. This section is also described later.

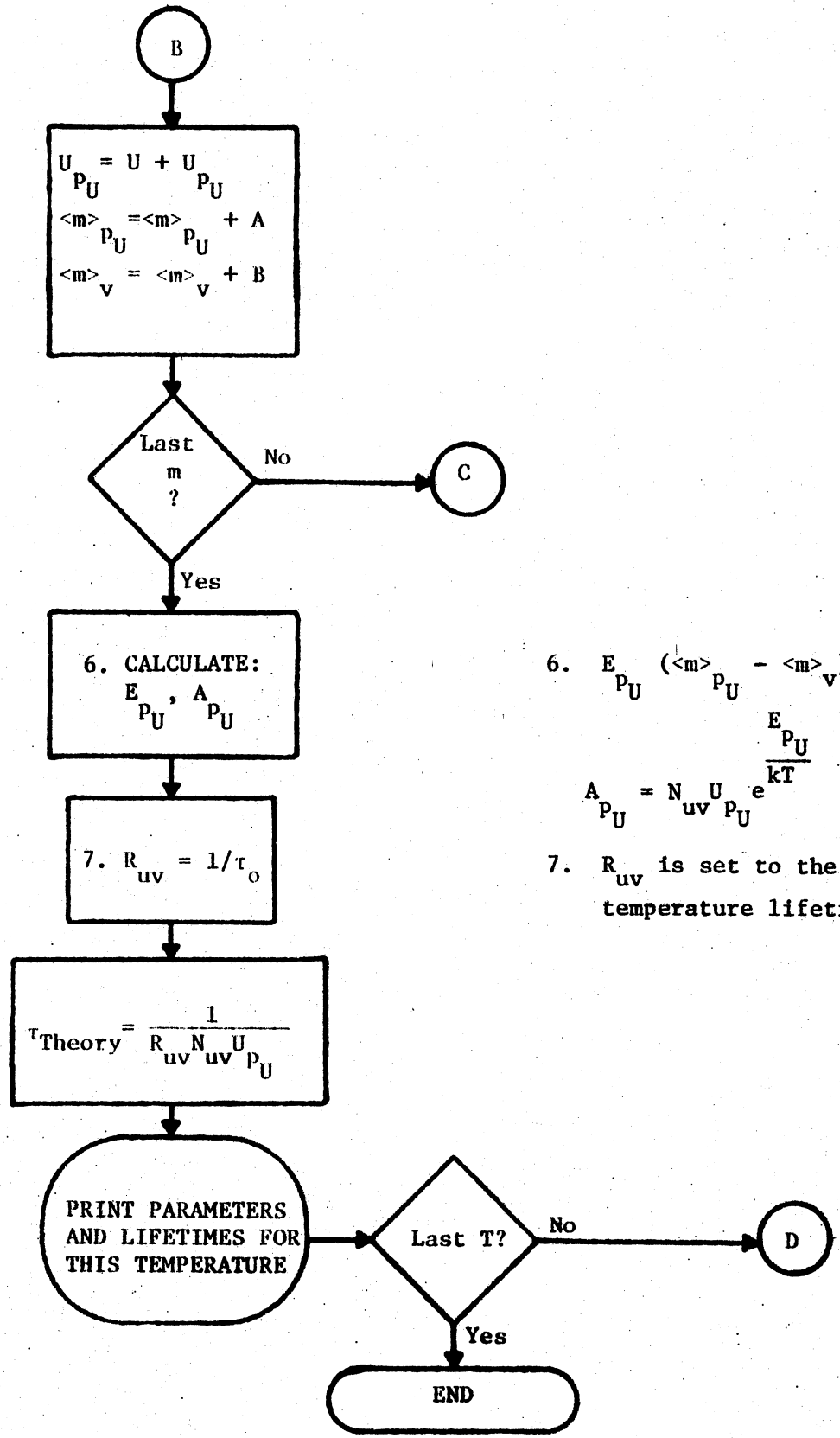

6. $E_{p_U} (\langle m \rangle_{p_U} - \langle m \rangle_v) \hbar\omega_v$

$$A_{p_U} = N_{uv} U_{p_U} e^{\frac{E_{p_U}}{kT}}$$

7. R_{uv} is set to the low temperature lifetime.

CALCULATION OF m_o (Step Four)

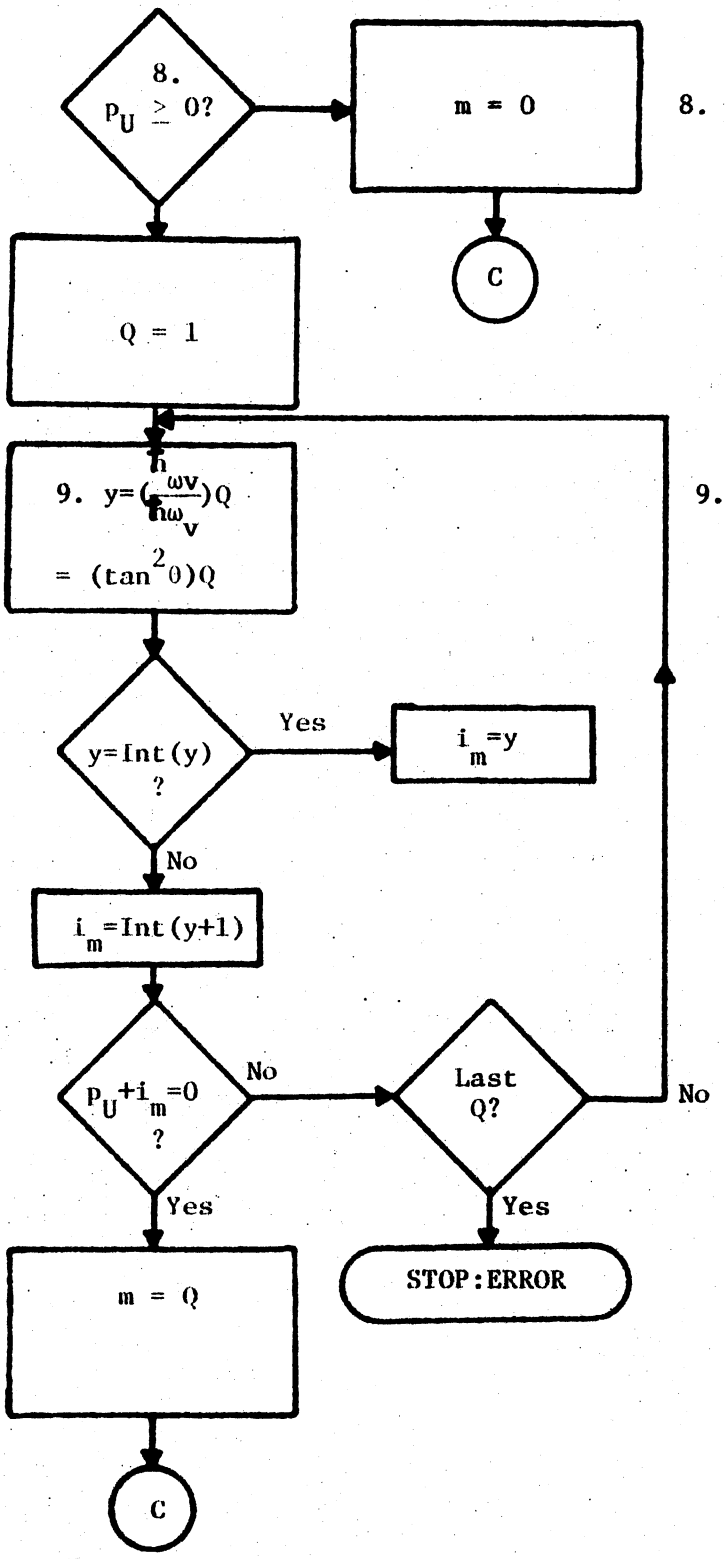

8. $m_o=0$ for $p_U \geq 0$, for p_U negative, m_o is the smallest m index for which $p_U+i_m=0$.

9. Since θ_2 and $h\omega_v$ are input the tan θ expression is simpler to use. Also note that the dummy variable Q is introduced for m.

CALCULATION OF i_m, f_m and $U^2_{p_U m}$ (Step Five)

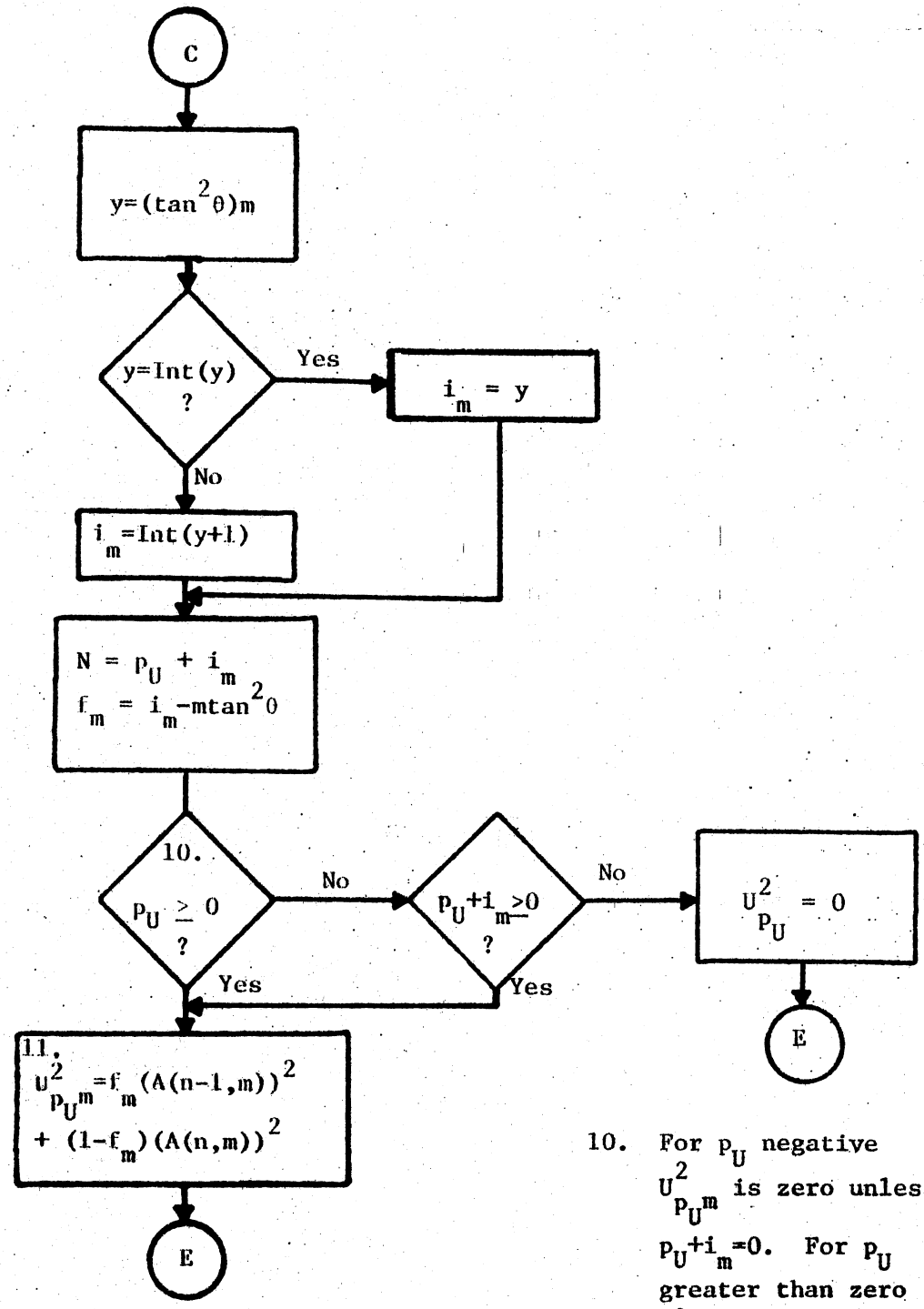

10. For p_U negative $U^2_{p_U m}$ is zero unless $p_U+i_m=0$. For p_U greater than zero $U^2_{p_U m}$ is given in box 11.

VITA[2]

Mark Vernon Iverson

Candidate for the Degree of

Doctor of Philosophy

Thesis: OPTICAL PROPERTIES OF $RbMnF_3:Er^{3+}$

Major Field: Physics

Biographical:

Personal Data: Born in Wisconsin Rapids, Wisconsin, August 17, 1953, son of Mr. and Mrs. Vernon C. Iverson; married Rachel Lynn Elson May 26, 1975; one son, Nathaniel Mark Iverson was born July 30, 1978.

Education: Graduated from John Edwards High School, Port Edwards, Wisconsin in 1971; received Bachelor of Arts degree in mathematics and physics from Luther College, Decorah, Iowa, in 1975; completed requirements for Doctor of Philosophy degree at Oklahoma State University, in July, 1979.

Professional Experience: Computer Process Control Engineer, Nekoosa-Edwards Paper Company, in January, 1975; Graduate Teaching Assistant for the Department of Physics at the Oklahoma State University, in 1975-1976; Graduate Research Assistant in the Department of Physics at Oklahoma State University, in summer 1976, summer of 1977, summer 1978, January 1979 through July 1979.